J. Fluid Mech. (2019), *vol.* 865, *pp.* 169–211.
doi:10.1017/jfm.2018.1023

Electric field mediated von Kármán vortices in stratified microflows: transition from linear instabilities to coherent mixing

Satarupa Dutta[1], Abir Ghosh[2], Partho Sarathi Gooh Pattader[1,2] and Dipankar Bandyopadhyay[1,2,†]

[1]Department of Chemical Engineering, Indian Institute of Technology Guwahati, Assam 781039, India

[2]Centre for Nanotechnology, Indian Institute of Technology Guwahati, Assam 781039, India

(Received 29 April 2018; revised 11 October 2018; accepted 14 December 2018; first published online 18 February 2019)

Application of an electric field across the pressure-driven stratified flow of a pair of miscible fluids inside a microchannel manifests interesting electrohydrodynamic (EHD) instabilities. Experiments uncover distinctive instability regimes with an increase in electric field Rayleigh number (Ra^{ψ}) – a linear-onset regime, a time-periodic nonlinear regime analogous to the von Kármán vortex street in the downstream and a regime with coherent flow patterns. The experiments also reveal that such linear and nonlinear instabilities can be stimulated non-invasively in a microchannel to mix or de-mix fluids simply by turning the electric field on or off, indicating the suitability of the process for on-demand micromixing. The characteristics of these instabilities have been theoretically investigated with the help of an Orr–Sommerfeld framework, which discloses the possibility of five distinctive finite-wavenumber modes for the instability. The EHD stresses originating due to the application of electric field stimulate a pair of shorter-wavelength electric field modes beyond a critical value of Ra^{ψ}. Increase in the levels of charge injection and EHD stresses lower the critical Ra^{ψ} of these modes. The relatively longer-wavelength viscous mode is found to appear when the viscosity stratification between the fluid layers is high. Beyond a threshold Schmidt number (Sc), a diffusive mode is also found to appear near the mixed interfacial region. A thinner interface between the fluids at a higher Sc helps this mode to behave as the interfacial mode of immiscible fluids. Contrast of ionic mobility in the fluids leads to the appearance of the K-mode of instability at much shorter wavelengths. The reported phenomena can be of significance in the domains of microscale mixing, pumping, heat exchange, mass transfer and reaction engineering.

Key words: absolute/convective instability, chaotic advection, microfluidics

1. Introduction

In recent years, the specialities of micro- and nanoscale science have been routinely exploited in diverse microfluidic applications such as cell cultures (Rhee *et al.* 2005), clinical diagnostics (Christodoulides *et al.* 2002), immunoassays (Wang *et al.*

† Email address for correspondence: dipban@iitg.ac.in

2001), DNA analysis (Doyle *et al.* 2002) and environmental monitoring (Bromberg & Mathies 2003). The microscale applications are found to have some distinct advantages over their macroscopic counterparts such as, (i) usage and control of lesser amounts of materials (Haeberle & Zengerle 2007); (ii) availability of higher surface to volume ratio; (iii) high performance due to process intensification (Mark *et al.* 2010); and (iv) superior control over the process parameters (Vilkner, Janasek & Manz 2004). It is now well understood that for efficient and time bound operations, the existing microscale chemical and biological applications require rapid mixing of fluid streams inside the microfluidic devices (Hertzog *et al.* 2006; Janasek, Franzke & Manz 2006; Samiei, Tabrizian & Hoorfar 2016). However, the conventional pressure-driven microfluidic flows are often limited by low values of the Reynolds number (*Re*), which results in large diffusive time and length scales of mixing owing to the dominance of the viscous force over the inertial one (Stroock *et al.* 2002; El Moctar, Aubry & Batton 2003). In the macroscopic processes, the diffusion limited mixing lengths are improved by the generation of auxiliary transport pathways such as turbulence. In contrast, for the microscale processes, the large frictional resistance originating from the confining boundaries pose multifarious challenges towards this end. Thus, of late, the enhancement of momentum, heat and mass transport in microscale processes has become one of the major areas of fluid dynamical research (Stone, Stroock & Ajdari 2004).

Over the years, various pathways have been explored to engender auxiliary transport mechanisms in microfluidic flows with the help of active and passive triggers. For example, the innovations associated with groovy or twisted channels (Bertsch *et al.* 2001; Stroock *et al.* 2002; Verma *et al.* 2008), multi-lamination of flow paths (Hinsmann *et al.* 2001), serpentine channels (Simonnet & Groisman 2005) and viscous fingering of fluids (Jha, Cueto-Felgueroso & Juanes 2011) disclose passive modes of enhanced momentum transport. In comparison, the active triggers require the support of the external fields such as applications of thermal (Wall & Wilson 1996), or acoustic waves (Rife *et al.* 2000), magnetic (Yi, Qian & Bau 2002), or electrokinetic forces (Oddy, Santiago & Mikkelsen 2001; Chen *et al.* 2005; Posner & Santiago 2006; Zhao & Bau 2007; Harnett *et al.* 2008; Posner, Pérez & Santiago 2012; Wang, Yang & Zhao 2014; Ding & Wong 2015; Wang *et al.* 2016). However, the enhancement of momentum, heat and mass diffusivities with the help of *in situ* disturbances inside microfluidic devices remains one of the long standing challenges in this regard. For example, the electrohydrodynamic (EHD) instabilities due to the electrokinetic phenomena instigated by conductivity gradients between the fluids have been explored only recently (Posner *et al.* 2012; Wang *et al.* 2014; Ding & Wong 2015; Wang *et al.* 2016).

In the present study, we investigate the consequence of an EHD phenomenon to develop laminar, transitional and chaotic flow regimes. The phenomenon originates due to injection of ions into a pair of miscible fluids undergoing a pressure-driven stratified flow in a microchannel. The miscible fluids are considered to have higher viscosity contrast and lower electrical conductivities to explore the cumulative effects of electric field stress and viscosity stratification. The major interests here are twofold: (i) to experimentally investigate the various regimes of instabilities in the aforementioned system leading to chaotic mixing of the fluid streams, and (ii) to theoretically analyse the linear regime of instability to predict their nature and onset conditions. The study is pertinent due to its significance in a plurality of futuristic applications such as microfluidic mixing in drug delivery systems, heat transfer enhancement, reactions in micro reactors, among others.

The prior art related to the stability of viscosity stratified miscible flows suggests that Craik (1969) was among the pioneers who identified that these flows can be more stable than the immiscible ones owing to the damping of the perturbations near the interface due to molecular diffusion. Much later, Ranganathan & Govindarajan (2001) theoretically identified the influence of the location of the viscosity stratified layer with respect to the critical layer of the perturbation. Subsequently, Ern, Charru & Luchini (2003) showed that the effect of molecular diffusion is not always stabilizing. They identified that for moderate values of Péclet number ($400 \leqslant Pe \leqslant 10\,000$), the perturbation at a thicker interface might grow to destabilize the system. Later, Govindarajan (2004) identified an overlap mode of instability, distinct from the classical Tollmien–Schlichting (TS) and inviscid modes, obtained when the critical layer of the most dominant disturbance merges with the viscosity stratified layer. More recently, Selvam *et al.* (2007, 2009) noted that miscible core–annular flows can be unstable beyond a critical viscosity ratio, when the lighter phase occupies the annular region. The observations in this study uncovered some of the exceptions to the claims of Ranganathan & Govindarajan (2001). Talon & Meiburg (2011) performed the stability analysis of miscible fluids with strong viscosity stratification in the Stokes flow regime ($Re \to 0$), and observed four distinct modes of instability in which two were interfacial while the other two were bulk modes. They proposed that these instabilities grew due to the phase shift between vorticity and interfacial perturbations. Subsequently, a number of works showed the influence of miscibility (Sahu & Govindarajan 2016), inclination (Scoffoni, Lajeunesse & Homsy 2001; d'Olce *et al.* 2009; Ghosh & Usha 2016) and variable density (Talon, Goyal & Meiburg 2013) on the different modes of instability. Apart from macroscopic flows, microscale flows of miscible fluids have also been explored theoretically (Tan & Homsy 1986; Preziosi, Chen & Joseph 1989; Chen & Meiburg 1996), as well as experimentally (Petitjeans & Maxworthy 1996; Lajeunesse *et al.* 1999). Interestingly, these studies indicate that the dominance (weakness) of the frictional (inertial) force at the microscale often disallows intermixing of the fluid layers to provide a kinetic stability at the stratified interface, even when the molecular diffusivities of the fluid layers are high, leading to a weaker capacity of heat, mass and momentum transfer.

In this regard, the use of an external electric field is found to be an efficient alternative to promote disturbance in various microfluidic flows. Previous studies indicate that various EHD phenomena can improve the performance of microscale electrowetting (Ko, Lee & Kang 2008), rheological devices (Otsubo & Edamura 1998), electrospinning (Skotak & Larsen 2006) and drug delivery systems (Chakraborty *et al.* 2009). In particular, the electroconvection inside a fluid originating from ionic or charge injections from an electrode to a dielectric fluid has attracted a lot of attention (Atten & Gosse 1969; Watson, Schneider & Till 1970; Hopfinger & Gosse 1971; Atten 1974; Lacroix, Atten & Hopfinger 1975; Denat, Gosse & Gosse 1979). In such processes, the electrical conduction is controlled by the creation of charge carriers at high electric field intensities through electrochemical reaction at the electrode–fluid interface for fluids having higher electrical resistivity (Alj *et al.* 1985; Suh 2012). The Coulomb force acting on the injected ions stimulate an auxiliary advection inside the fluidic medium (Malraison & Atten 1982; Oliveri, Atten & Castellanos 1987; Castellanos 1991) to enhance momentum, heat and mass transfer (McCluskey, Atten & Perez 1991; Allen & Karayiannis 1995) as well as throughputs (Bart *et al.* 1990).

The onset of electroconvection in fluid flows has been traditionally analysed from the magnitudes of the following dimensionless numbers, (i) electric field Rayleigh number $Ra^{\psi}(=(\varepsilon\Psi_0/K\mu))$ – the ratio of Coulombic to viscous force and (ii) injection

level $I^q(=(Q_0L^2/\varepsilon\Psi_0))$. Here, the notations ε, Ψ_0, K, μ, Q_0 and L denote electrical permittivity, applied voltage, ionic mobility, fluid viscosity, volumetric charge density at the injecting electrode and distance between the electrodes respectively. The instability of dielectric quiescent fluids subjected to unipolar ion injections was first reported by Schneider & Watson (1970) neglecting the effects of diffusion. Subsequently, Watson *et al.* (1970), performed an experimental analysis by creating strong ion injections ($I^q \gg 1$) on the surface of a liquid with an electron beam, identifying the critical voltage Ψ_0, for onset of electroconvection to be approximately 99. Later, Atten & Moreau (1972) established for the case of weak injections ($I^q \ll 1$), a stability criterion of $Ra^{\psi}I^{q2} = 220.7$, whereas for strong injections ($I^q \gg 1$) the stability criterion was defined by $Ra^{\psi} = 160.75$. However, the experiments performed by Atten & Lacroix (1979) reported the critical Ra^{ψ} to be 100 for the space charge limited regime. Following this, a number of analytical and numerical investigations of the process of electroconvection due to the unipolar injection of ions have been reported by many groups (Vázquez, Georghiou & Castellanos 2006; Traoré & Pérez 2012; Wu *et al.* 2013, 2015; Zhang *et al.* 2015; Wang & Sheu 2016; Zhang 2016).

The literature discussed so far indicate that, while the contributions of inertial and molecular diffusive forces have been explored in detail in the past, arguably, there is no report as such of the influence of electric field induced instabilities on stratified two-layer miscible flows inside microchannels. In the present study, with the help of combined experimental as well as theoretical analyses, the effects of electroconvection on a two-layer viscosity stratified miscible flow inside a microchannel have been explored. We report the experimental investigations of the various regimes of instabilities produced due to ion injections from electrodes into a viscosity stratified flow of miscible fluids, which subsequently lead to the coherent mixing of the fluid streams. Experiments uncover three different instability regimes with an increase in electric field intensity, namely, a linear-onset regime, time-periodic nonlinear regime with the formation of von Kármán vortices and a chaotic flow regime. An Orr–Sommerfeld analysis of the governing equations with appropriate boundary conditions has also been performed to identify the various linear modes of instabilities of the system, which helps in the identification of the onset conditions of the EHD instabilities.

The paper is organized as follows. Section 2 contains a description of the experimental methodology, in § 3 the mathematical formulation is shown along with the linear stability equations, and solutions of the base states. Section 4 covers the experimental and theoretical results. Section 5 contains the conclusions from the analysis.

2. Experiment

2.1. *Materials and methods*

Experiments were carried out in a cylindrical microchannel of 420 μm diameter built on a PDMS (poly-dimethylsiloxane) platform. The channels were fabricated by template moulding technique (Timung *et al.* 2017) employing a silicone elastomer (SLYGARD 184 silicone elastomer, Dow Corning). For the fabrication of the channels, templates were first prepared with the help of copper wires (Cu) of the same dimension, as required for the channel. A rectangular well was then formed with double sided tapes, with the Cu wire template fixed into the well. Liquid PDMS mixed with a cross-linker in the ratio 10 : 1 was then poured inside the well before curing the system in a vacuum oven at 80 °C for 2 h. The template was then

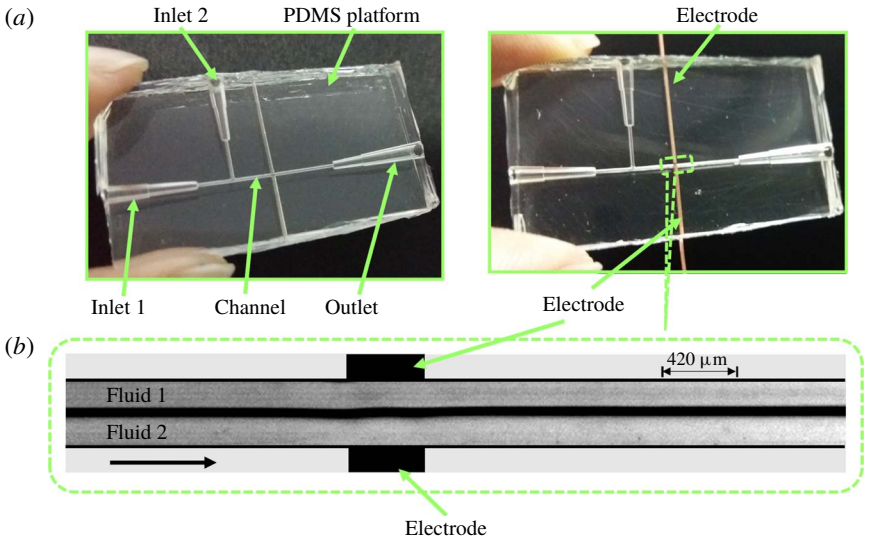

FIGURE 1. (Colour online) (*a*) Shows the top view of the experimental microchannel on a poly-dimethylsiloxane (PDMS) platform. Fluids 1 and 2 with viscosities μ_1 and μ_2 ($\mu_2 > \mu_1$), respectively, enter the channel through their respective inlets, and are then subjected to an electric field applied from a direct current (DC) high voltage source through Cu wire electrodes as shown. (*b*) Shows the experimental micrograph of the top view of the region marked in (*a*). Fluids 1 and 2 form a stratified flow in the channel (side by side), and are subjected to an electric field via Cu wire electrodes. The diameter of the channel and the electrodes are 420 μm. The average *Re* of the flow is maintained at 0.5. The arrow in (*b*) indicates the direction of the flow.

pulled out of the solid PDMS block to form the channels of required configuration. The Cu wire electrodes of 420 μm diameter were integrated across the channel wall, for application of electric field potential. Experiments were conducted using different liquid pairs. Benzene (analytical grade, procured from Merck Ltd. (India), viscosity, $\mu_1 \approx 0.603$ cP at 25 °C; dielectric constant, $\varepsilon_{r1} \approx 2.284$ (van der Maesen 1949)) formed the lower viscosity phase. Oleic acid (analytical grade, procured from Merck Ltd. (India), viscosity, $\mu_2 \approx 18$ cP at 25 °C; dielectric constant, $\varepsilon_{r2} \approx 2.32$ (de Sousa *et al.* 2009)), silicone oil (analytical grade, procured from Merck Ltd. (India), viscosity, $\mu_2 \approx 317$ cP at 25 °C; dielectric constant, $\varepsilon_{r2} \approx 2.5$ (Ren, Wang & Huang 2016)) and soybean oil (procured from local vendor, viscosity, $\mu_2 \approx 50$ cP at 25 °C; dielectric constant, $\varepsilon_{r2} \approx 3.3$ (Spohner 2016)) formed the higher viscosity phases. The viscosities of the liquids were measured using interfacial rheometer (Anton Paar, Physica MCR 301).

Figure 1(*a*) shows photographs of the experimental channel, before and after electrode integration. The two liquids flowed through the inlets 1 and 2 of the PDMS channel with the help of a syringe pump (Harvard Apparatus, PHD 2000). Electric field was applied from a high voltage direct current (DC) source (SES Instruments Pvt. Ltd, EHT-II) via Cu wire electrodes of 420 μm diameter as shown figure 1(*a*). The flow of the liquids through the channel was recorded with a high speed camera (Photron, Fastcam Mini UX-100). A picoammeter (SES Instruments Pvt. Ltd, Model DPM-111) was used to measure the electric current across the electrodes. Figure 1(*b*) demonstrates the experimental micrograph of the highlighted portion in figure 1(*a*),

which shows the stratified flow of fluids 1 and 2 in absence of an electric field. Before and after every experiment the channels were first cleaned by ultra-sonication in an acetone bath for 10 min. It was followed by treatment with 10 % V/V dilute piranha solution ($H_2SO_4 : H_2O_2$, 3 : 1) for 15 min. The channels were then repeatedly washed with deionized water (Merck Millipore, grade I), dried by blowing nitrogen gas, and kept in an air oven at 70 °C for 20 min.

2.2. *Calculation of injection level*

Previous studies indicate that strong unipolar injections ($I^q \gg 1$) with space charge limited currents can be achieved experimentally by covering the electrodes with suitable perm-selective membranes and varnishes (Atten & Gosse 1969; McCluskey & Atten 1988). In comparison, for non-polar liquids, moderate and weak injections have been achieved by doping the liquids with appropriate salts (Denat *et al.* 1979; Pontiga, Castellanos & Malraison 1995). It has also been shown that intense localized injections of charge can be achieved by concentrating the electric field with the use of blade or needle electrodes (Tobazeon, Haidara & Atten 1984; Atten & Haidara 1985; Higuera 2002; Tsukahara, Hirose & Otsubo 2013). In the reported experiments, a DC voltage was applied from a high voltage source with the help of wire electrodes for the injection of charge into the dielectric experimental fluids. Since the electrodes were in contact with the experimental fluids, the injection of charge in the regions of high electric field was inevitable (Vasilkov, Chirkov & Stishkov 2017). In order to measure the injection level, a stratified flow of the lower viscosity phase, composed of benzene, and higher viscosity phase, composed of oleic acid (or silicone oil), was maintained in the microchannel with the help of a syringe pump. DC voltage input was applied to the system with the help of the copper wire electrodes, while the electric current was measured across the electrodes with the help of a picoammeter. The current–voltage curves for the cases: (i) benzene–oleic acid and (ii) benzene–silicone oil are shown in figure 2. The electric field intensity between the electrodes was obtained by dividing the applied voltage by the distance between the electrodes (420 μm). The value of electric current across the electrodes was recorded for each applied voltage across each liquid separately before the same was repeated for the stratified flows. It has been shown in previous literature that for electric fields within the range $5 \times 10^2 \leqslant E \leqslant 5 \times 10^4$ kV cm^{-1}, the charge density at the injector remains almost constant and independent of the electric field (Castellanos 1991). Hence, the assumption of autonomous injection for the present analysis seems to be reasonably valid. The measured electrical current in the quiescent liquid is due to the contribution of two processes: (i) residual conduction and (ii) migration of injected ions (Denat *et al.* 1979; McCluskey *et al.* 1991). Previously, Denat *et al.* (1979) showed that the conduction current can be considered negligible if the ratio of conduction current to injection current, $C_0 (= (\sigma L^2/2K\varepsilon\Psi_0))$, is less than 0.5. The working liquids benzene and oleic (or silicone oil) acid have conductivities of the order of $\sim 10^{-13}$ Sm^{-1} (Bobyl, Romanets & Alyab'ev 1965; Zhang, Edirisinghe & Jayasinghe 2006), while the value of ionic mobility K in the working liquids is of the order of $\sim(10^{-8}$–$10^{-10})$ m^2 s^{-1} V^{-1} (Denat *et al.* 1979). In such a situation, the value of C_0 was found to be less than 0.5 for the experiments reported in the present work. Thus, the total current was considered to be due to ionic injections from the electrodes only. Thereafter, the injection level I^q was calculated from (3.9), using the current voltage curves shown in figure 2. The injection levels I^q for the experiments shown in the present study were found to be in the range of 0.5–1.15, indicating a moderate injection.

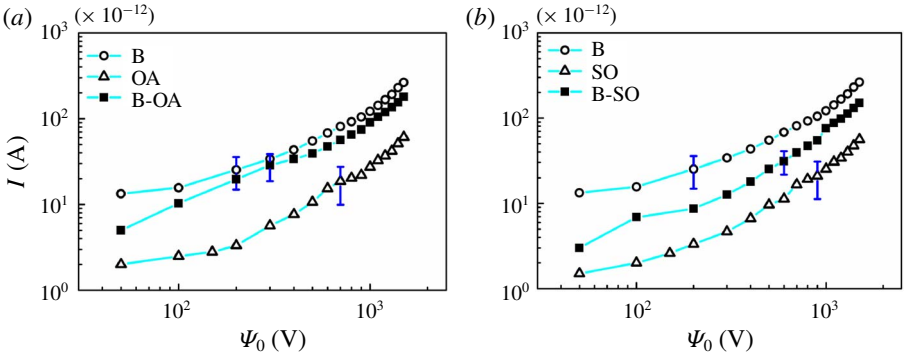

FIGURE 2. (Colour online) (*a,b*) Show the current (I) versus voltage (Ψ_0) curves for different combinations of flows. (*a*) Shows the combination of single component flows of benzene (B), oleic acid (OA) and a stratified flow of benzene and oleic acid (B-OA). (*b*) Shows the combination of single component flows of benzene (B), silicone oil (SO) and a stratified flow of benzene and silicone oil (B-SO). The error bar represents the maximum standard deviation obtained from three experiments.

3. Theoretical formulation

3.1. *Problem formulation*

The experiments were carried out in a cylindrical microchannel (420 μm diameter) as already discussed in § 2.1. To gain in-depth information about the nature and onset conditions of the reported EHD instabilities, a scrupulous investigation considering a similar flow geometry to the experimental channel is required. However, the mathematical treatment of the problem considering a cylindrical coordinate system is seemingly cumbersome, especially because the experimental flow configuration is non-axisymmetric, due to integration of the electrodes on the channel walls. This calls for a complete three-dimensional formulation of the problem in the cylindrical coordinate system followed by a global stability analysis, which in the context of the reported problem will be extremely involved. We thus resorted to a two-dimensional planar geometry. Figure 3(*a*) depicts the laminar flow of a pair of miscible fluids flowing through a channel, before being subjected to a DC voltage Ψ_0. A Cartesian coordinate system is chosen as the reference frame with the x and z axes perpendicular to each other on the same plane. The distance between the two electrodes is $2R$, while the electric field is applied in the z direction. The fluids, namely, fluid 1 of viscosity μ_1 and fluid 2 of viscosity μ_2 ($\mu_2 > \mu_1$), are assumed to be of equal density, and dielectric permittivity, and the ionic mobility is considered to be the same in both fluids. For two miscible fluids flowing inside a microchannel, the associated mass transfer Péclet number [$Pe = ul/\kappa$], is of the order of $\sim 10^2$ or higher (Stroock *et al.* 2002), leading to a slow diffusive mixing between the fluids. Thus, in the present study, which is motivated by flows inside microchannels, the thickness of the mixed interface can be effectively assumed to be constant. The interface between the two fluids grows diffusively to a distance δ in such a manner that fluid 1 occupies the region $h + \delta/2 \leqslant z \leqslant R$ and fluid 2 occupies the region $-R \leqslant z \leqslant h - \delta/2$, where h is the distance of the mixed interface from the datum line $z = 0$.

The viscosity of the fluids is formulated as an exponential function of the concentration scalar S, such that the base values of the scalar S_0 are 0 and 1 in

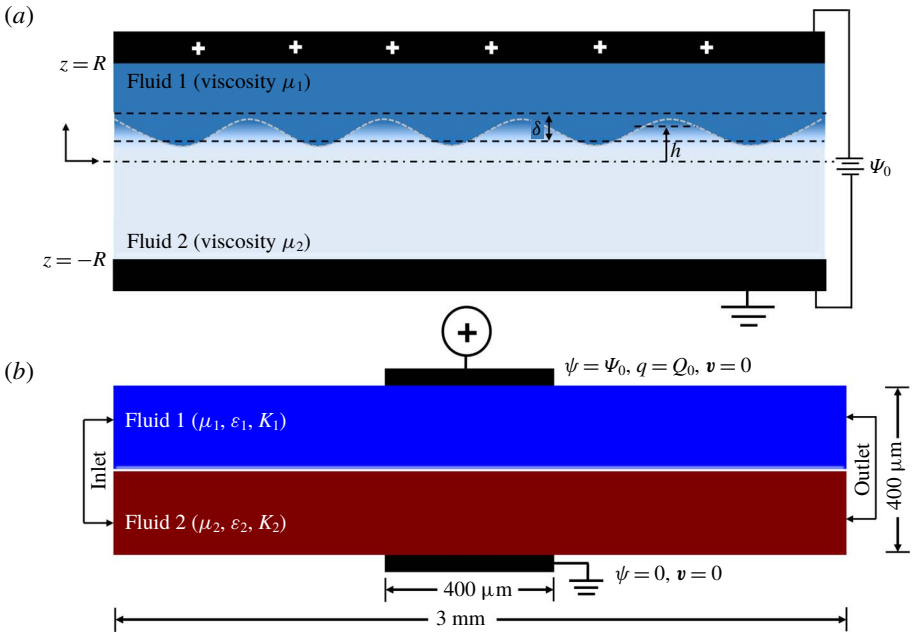

FIGURE 3. (Colour online) Schematic illustration of (*a*) the theoretical framework for the linear stability analysis. Two miscible fluids 1 and 2 with viscosities μ_1 and μ_2 ($\mu_2 > \mu_1$), respectively, form a stratified flow. The diffuse interface between them is of width δ, and located at a distance h from the datum line, $z = 0$. The fluids are subjected to an electric potential of Ψ_0, applied through the electrodes separated by a distance of $2R$, where R is half the channel width. (*b*) The computational domain for the nonlinear computational fluid dynamics (CFD) simulations.

the top and bottom layers, respectively. The viscosity μ is modelled as,

$$\mu = \mu_1 \exp(SV^L), \tag{3.1}$$

where, V^L is the log viscosity ratio of the fluids defined as, $V^L = \ln(\mu_2/\mu_1)$ (Sahu & Govindarajan 2016). The Reynolds number (Re) is defined as $Re = Q/R\eta_1$, where Q is the volumetric flow rate and η_1 is the kinematic viscosity of fluid 1. In order to bring about homogeneity between the theoretical and experimental analyses, the strength of injection, characterized by the injection parameter, I^q, is calculated experimentally (refer to § 2.2), and used for the theoretical analysis. It is observed that the injection is homogeneous and autonomous in the experiments. Assuming a medium injection level, the value of the injection parameter, I^q, is fixed at 1 for the theoretical analysis unless otherwise stated. In the formulation, 't' represents time, the bold variables indicate vectors and the dashed variables denote derivative with respect to 'z'.

3.2. *Governing equations*

The fluids are assumed to be Newtonian and incompressible, thereby the flow field can be defined by the following continuity and momentum equations neglecting the effect of gravity,

$$\boldsymbol{\nabla} \cdot \boldsymbol{v} = 0, \tag{3.2}$$

$$\rho\left(\frac{\partial \boldsymbol{v}}{\partial t}+\boldsymbol{v}\cdot\boldsymbol{\nabla}\boldsymbol{v}\right)=-\boldsymbol{\nabla}p+\boldsymbol{\nabla}\cdot[\mu(\boldsymbol{\nabla}\boldsymbol{v}+\boldsymbol{\nabla}\boldsymbol{v}^{\mathrm{T}})]+\boldsymbol{F}_e. \tag{3.3}$$

Where $\boldsymbol{v}$ is the velocity vector, ρ is the density, p is the pressure and $\boldsymbol{F}_e$ is the electrical body force term given by,

$$\boldsymbol{F}_e=q\boldsymbol{E}-\frac{1}{2}|\boldsymbol{E}|^2\boldsymbol{\nabla}\varepsilon+\boldsymbol{\nabla}\left(\rho\frac{|\boldsymbol{E}|^2}{2}\frac{\partial\varepsilon}{\partial\rho}\right). \tag{3.4}$$

Here, q represents the volumetric charge density, $\boldsymbol{E}$ is the electric field intensity and ε is the electrical permittivity. The first term of (3.4) represents the Coulomb force exerted by the electric field on the free charges, and is generally the strongest in case of a DC supplied voltage. The second term of (3.4) is the dielectric force exerted by the electric field on the bound charges, and is neglected in the present analysis due to the negligible gradient of dielectric permittivity. The third term of (3.4) is the electrostrictive force which is included with the pressure term of the Navier–Stokes equation. The irrotational electric field $\boldsymbol{E}$ is assumed to follow the field, $\boldsymbol{E}=-\boldsymbol{\nabla}\psi$, which leads to the following Poisson's equation originating from the governing Gauss's law in which the electric field potential is defined as ψ,

$$q=\boldsymbol{\nabla}\cdot\varepsilon\boldsymbol{E}, \tag{3.5}$$

$$\nabla^2\psi=-\frac{q}{\varepsilon}. \tag{3.6}$$

The continuity equation for charge density is given by,

$$\frac{\partial q}{\partial t}+\boldsymbol{\nabla}\cdot\boldsymbol{J}=0, \tag{3.7}$$

where, the current density $\boldsymbol{J}$ is given by,

$$\boldsymbol{J}=q\boldsymbol{v}+qK\boldsymbol{E}-D\boldsymbol{\nabla}q+\sigma\boldsymbol{E}. \tag{3.8}$$

The first term of (3.8) accounts for the convection of charges due to motion of the fluid moving with a velocity $\boldsymbol{v}$. The second term accounts for the drift transport of charges under the effect of the electric field, where K is the mobility of the ions moving with velocity $K\boldsymbol{E}$. The third term accounts for the diffusive transport of the ions with diffusion coefficient D, which is neglected because of its smaller magnitude as compared to the other terms (Lacroix *et al.* 1975; Denat *et al.* 1979; Castellanos 1991). In the present analysis, the fluids under study are considered to be nearly electrically non-conductive ($\sigma\leqslant 10^{-13}$ Sm^{-1}), thereby making the last term of (3.8) negligible. Therefore, the constitutive relation for current density reduces to,

$$\boldsymbol{J}=q\boldsymbol{v}+qK\boldsymbol{E}. \tag{3.9}$$

Substituting (3.9) into (3.7), and using (3.2), we obtain the conservation equation for the charge density as,

$$\frac{\partial q}{\partial t}+\boldsymbol{v}\cdot(\boldsymbol{\nabla}q)+K[q(\boldsymbol{\nabla}\cdot\boldsymbol{E})+\boldsymbol{E}\cdot(\boldsymbol{\nabla}q)]=0. \tag{3.10}$$

The advection–diffusion equation for the concentration scalar S gives,

$$\frac{\partial S}{\partial t}+\boldsymbol{v}\cdot\boldsymbol{\nabla}S=\kappa\nabla^2S. \tag{3.11}$$

Here, κ is the diffusion coefficient of the scalar. For the velocity field, no-slip and no-penetration boundary conditions are enforced at the channel walls, i.e. $[\boldsymbol{v}(\pm R)=0,\ \boldsymbol{v}'(\pm R)=0]$. The boundary conditions used to solve for the electric potential ψ are: $\psi(R)=\Psi_0,\ \psi(-R)=0$.

3.3. *Non-dimensional governing equations*

The equations are reduced to dimensionless forms by using the following scheme,

$$\left.\begin{gathered}(x, z, h, \delta) = R(x^*, z^*, h^*, \delta^*), \quad (u, w) = \frac{K\Psi_0}{R}(u^*, w^*), \quad \psi = \Psi_0\psi^*, \\ q = Q_0 q^*, \quad t = \frac{R^2}{K\Psi_0}t^*, \quad p = \frac{\rho K^2\Psi_0^2}{R^2}p^*, \quad \mu = \mu_1\mu^*.\end{gathered}\right\} \tag{3.12}$$

The asterisk symbol depicts dimensionless quantities. Here, Ψ_0 and Q_0 represent the applied voltage and the charge density at the injector, respectively. The dimensionless governing equations after dropping the asterisk symbol are,

$$\nabla \cdot \boldsymbol{v} = 0, \tag{3.13}$$

$$\frac{\partial \boldsymbol{v}}{\partial t} + \boldsymbol{v} \cdot \nabla \boldsymbol{v} = -\nabla p + \frac{1}{Re^{\psi}}\nabla \cdot [\mu(\nabla \boldsymbol{v} + \nabla \boldsymbol{v}^{\mathrm{T}})] + I^q {R_M}^2 (q\boldsymbol{E}), \tag{3.14}$$

$$\nabla^2 \psi = -I^q q, \tag{3.15}$$

$$\frac{\partial q}{\partial t} + \boldsymbol{v} \cdot (\nabla q) + q(\nabla \cdot \boldsymbol{E}) + \boldsymbol{E} \cdot (\nabla q) = 0, \tag{3.16}$$

$$\frac{\partial S}{\partial t} + \boldsymbol{v} \cdot \nabla S = \frac{1}{Re^{\psi} Sc}\nabla^2 S, \tag{3.17}$$

where,

$$Re^{\psi} = \frac{K\Psi_0}{\eta_1}, \quad R_M = \frac{(\varepsilon/\rho)^{1/2}}{K}, \quad I^q = \frac{Q_0 R^2}{\varepsilon\Psi_0}, \quad Sc = \frac{\eta_1}{\kappa}. \tag{3.18a–d}$$

Here, Re^{ψ} is defined as the electric Reynolds number, R_M is defined as the ratio between the hydrodynamic mobility $[(\varepsilon/\rho)^{1/2}]$ and the true ionic mobility K, I^q is the charge injection level and Sc is the Schmidt number. The electric field Rayleigh number Ra^{ψ} is defined as $Ra^{\psi} = Re^{\psi}{R_M}^2 = (\varepsilon\Psi_0)/(\mu_1 K)$, and gives the ratio of the electrostatic to viscous force. The non-dimensional boundary conditions used to solve the velocity field are: $\boldsymbol{v}(\pm 1) = 0$, $\boldsymbol{v}'(\pm 1) = 0$. For the solution of the electric potential ψ, the non-dimensional boundary conditions used are: $\psi(1) = 1$, $\psi(-1) = 0$, $\psi''(1) = -I^q$.

3.4. *Linear stability*

A general linear stability analysis (LSA) has been carried out by splitting the flow and electric field variables into base-state and perturbed-state quantities. We consider only the transverse modes because the existing literature suggests that the longitudinal modes remain unaffected by the parallel shear flow or the other parameters of interest reported in the present study (Castellanos & Agrait 1992; Lara, Castellanos & Pontiga 1997; Sahu & Govindarajan 2016). In such a scenario a two-dimensional (2-D) stability analysis is found to be sufficient to qualitatively uncover the underlying physics and predict the onset conditions. The formulation considering three-dimensional (3-D) perturbations is also shown in appendix B. The governing equations are linearized considering the following linear modes:

$$\begin{aligned}[u, w, p, \psi, S, \mu](x, z, t) \; = \; & [u_0(z), 0, p_0, \psi_0(z), S_0(z), \mu_0(z)] \\ & + [\tilde{u}, \tilde{w}, \tilde{p}, \tilde{\psi}, \tilde{S}, \tilde{\mu}](z)\mathrm{e}^{(\omega t + \mathrm{i}kx)}.\end{aligned} \tag{3.19}$$

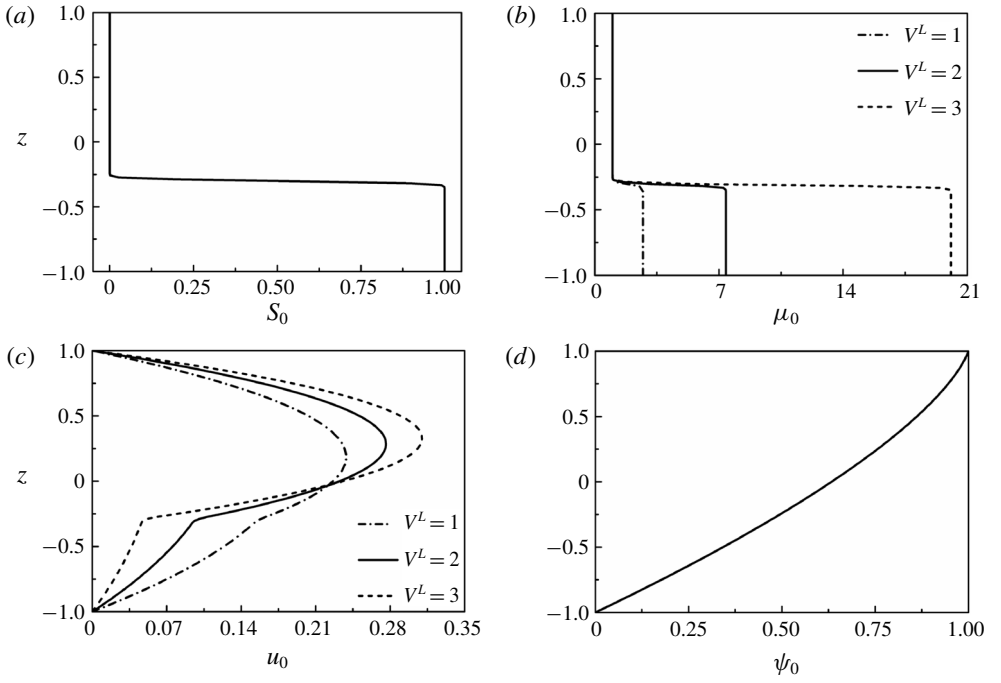

FIGURE 4. Base-state profiles for (*a*) concentration scalar S_0, (*b*) viscosity μ_0, (*c*) velocity u_0 and (*d*) potential ψ_0, for $h = -0.3$ and $\delta = 0.02$.

The variables with subscript '0' denote the base-state quantities and the variables with 'tilde' are the perturbed quantities. Here, u and w are the x and z directional velocities, respectively. The symbols ω and k are the growth coefficient and the wavenumber of the perturbation, respectively. The parameter ω is a complex quantity ($\omega = \omega_r + \mathrm{i}\omega_i$). A perturbation is unstable when $\omega_r > 0$, stable when $\omega_r < 0$, and neutrally stable when $\omega_r = 0$. The perturbation viscosity $\tilde{\mu}$ is modelled as, $\tilde{\mu} = (\mathrm{d}\mu_0/\mathrm{d}S_0)\tilde{S}$ (Sahu & Govindarajan 2016).

3.4.1. *Base-state analysis*

It is assumed that the diffusive interface between the two miscible fluids is of thickness δ. If $\delta \ll 1$, then the base-state profile of the concentration scalar can be estimated following a quasi-steady approximation [$\omega \gg \kappa/\delta^2$] (Tan & Homsy 1986; Selvam *et al.* 2007) as,

$$S_0 = 0.5 - 0.5\mathrm{erf}\left(\frac{z-h}{\delta}\right). \tag{3.20}$$

Here, the variable, h, is the dimensionless distance of the diffused interface from the datum, $z = 0$. The base-state profile of the concentration scalar is shown in figure 4(*a*). The base-state profiles for viscosity μ_0, are then obtained from the relation,

$$\mu_0 = \exp(S_0 V^L). \tag{3.21}$$

The base-state velocity profile u_0 is then obtained by solving (3.14) for steady state, after dropping the electrical body force term, which gives,

$$\mu_0(u_0'' + V^L u_0' S_0') = Re^{\psi}\frac{\mathrm{d}p_0}{\mathrm{d}x}. \tag{3.22}$$

Equation (3.22) is solved with no-slip boundary conditions at the channel walls, $u_0(\pm 1) = 0$, in which the non-dimensional pressure gradient, $(\mathrm{d}p_0/\mathrm{d}x)$, is fixed by assuming a constant volumetric flow rate. From (3.16) the base state equation for electric potential is obtained as,

$$(\psi_0'')^2 + \psi_0'\psi_0''' = 0. \tag{3.23}$$

Equation (3.23) is solved numerically with the boundary conditions: $[\psi_0(1) = 1;\ \psi_0(-1) = 0;\ \psi_0''(1) = -I^q]$. The base-state profiles for viscosity (μ_0), velocity (u_0) and electric potential (ψ_0) are shown in figure 4(*a–d*). Panel (*a*) of this figure shows that S_0 is zero at layer 1 and it is one at layer 2 while the variation across the diffused interface is sharp but continuous. A similar trend of the variation in the dimensionless viscosity μ_0 can also be seen in (*b*). Further, (*c*) shows the dimensionless velocity profile u_0 of the base state under varied conditions. Panel (*d*) shows the variation of the base-state electric field potential, ψ_0, across the fluid layers.

3.4.2. *Perturbed-state analysis*

The governing equations (3.13)–(3.17) are perturbed with the variables mentioned in (3.19) in which the growth coefficient, ω, is represented in terms of the wave speed c as, $\omega = -\mathrm{i}kc$. The dimensionless linearized equations of motion and continuity equation after eliminating the pressure perturbation term are given by,

$$\begin{aligned} &Re^{\psi}\mathrm{i}k[(u_0 - c)(\tilde{w}'' - k^2\tilde{w}) - u_0''\tilde{w}] + Ra^{\psi}k^2[\psi_0'\tilde{\psi}'' - (\psi_0''' + k^2\psi_0')\tilde{\psi}] \\ &\quad = \mu_0\tilde{w}'''' + 2\mu_0'\tilde{w}''' + (\mu_0'' - 2k^2\mu_0)\tilde{w}'' - 2k^2\mu_0'\tilde{w}' + (k^2\mu_0'' + k^4\mu_0)\tilde{w} \\ &\qquad - \mathrm{i}ku_0'\tilde{\mu}'' - 2\mathrm{i}ku_0''\tilde{\mu}' - (\mathrm{i}ku_0''' + \mathrm{i}k^3u_0')\tilde{\mu}. \end{aligned} \tag{3.24}$$

Equations (3.16) and (3.17) reduce to the following equations,

$$\begin{aligned} \mathrm{i}k\left[(u_0 - c)(\tilde{\psi}'' - k^2\tilde{\psi}) - \frac{\mathrm{i}}{k}\psi_0'''\tilde{w}\right] &= \psi_0'\tilde{\psi}''' + 2\psi_0''\tilde{\psi}'' + (\psi_0''' - k^2\psi_0')\tilde{\psi}' \\ &\quad - 2k^2\psi_0''\tilde{\psi}, \end{aligned} \tag{3.25}$$

$$\mathrm{i}kRe^{\psi}Sc\left[(u_0 - c)\tilde{S} - \frac{\mathrm{i}}{k}S_0'\tilde{w}\right] = \tilde{S}'' - k^2\tilde{S}. \tag{3.26}$$

The boundary conditions employed to solve (3.24)–(3.26) are,

$$\tilde{w}(\pm 1) = 0, \quad \tilde{w}'(\pm 1) = 0, \tag{3.27a,b}$$

$$\tilde{\psi}(\pm 1) = 0, \quad \tilde{\psi}''(1) = 0, \tag{3.28a,b}$$

$$\tilde{S}'(\pm 1) = 0. \tag{3.29a,b}$$

3.4.3. *Numerical method*

The domain is discretized employing a spectral collocation method based on Chebyshev polynomials (Orszag 1971; Weideman & Reddy 2000). The three ordinary differential equations defined by (3.24)–(3.26) reduce to the following eigenvalue form upon discretization,

$$\boldsymbol{A}\tilde{\phi} = \omega \boldsymbol{B}\tilde{\phi}, \tag{3.30}$$

where $\boldsymbol{A}$ and $\boldsymbol{B}$ are 3×3 matrices, given by,

$$\boldsymbol{A} = \begin{bmatrix} A_{11} & A_{12} & A_{13} \\ -Re^{\psi} Sc S_0' & A_{22} & 0 \\ -\psi_0''' & 0 & A_{33} \end{bmatrix}, \tag{3.31}$$

$$\boldsymbol{B} = \begin{bmatrix} Re_{\psi}(D_2 - k^2) & 0 & 0 \\ 0 & Re^{\psi} Sc & 0 \\ 0 & 0 & (D_2 - k^2) \end{bmatrix}, \tag{3.32}$$

and,

$$\tilde{\phi} = \begin{bmatrix} \tilde{w} \\ \tilde{S} \\ \tilde{\psi} \end{bmatrix}. \tag{3.33}$$

Here, $D_1 = \mathrm{d}/\mathrm{d}z$, $D_2 = \mathrm{d}^2/\mathrm{d}z^2$, $D_3 = \mathrm{d}^3/\mathrm{d}z^3$, $D_4 = \mathrm{d}^4/\mathrm{d}z^4$ and

$$\left.\begin{aligned} A_{11} &= \mu_0 D_4 + 2\mu_0' D_3 + (\mu_0'' - \mathrm{i}kRe^{\psi} u_0 - 2k^2\mu_0) D_2 - 2k^2\mu_0' D_1 \\ &\quad + \mathrm{i}k\left(Re^{\psi} u_0'' + \frac{k}{\mathrm{i}}\mu_0'' + Re^{\psi} k^2 u_0 + \frac{k^3}{\mathrm{i}}\mu_0\right), \\ A_{12} &= -\mathrm{i}kV^L \mu_0 u_0' D_2 - 2\mathrm{i}kV^L(\mu_0 u_0'' + u_0'\mu_0') D_1 \\ &\quad - \mathrm{i}kV^L(\mu_0 u_0''' + k^2\mu_0 u_0' + u_0'\mu_0'' + 2u_0''\mu_0'), \\ A_{13} &= Ra^{\psi} k^2(\psi_0'''' + k^2\psi_0' - \psi_0' D_2), \\ A_{22} &= D_2 - k^2 - \mathrm{i}kRe^{\psi} Sc u_0, \\ A_{33} &= \psi_0' D_3 + (2\psi_0'' - \mathrm{i}ku_0) D_2 + (\psi_0''' - k^2\psi_0') D_1 - 2k^2\psi_0'' + \mathrm{i}k^3 u_0. \end{aligned}\right\} \tag{3.34}$$

The eigenvalue problem defined by (3.30) has been solved with the help of a MATLAB code to obtain the variation in the growth rate, ω, with the wavenumber, k, for the unstable modes. In general, it is a common practice to cluster the grid in the viscosity stratified region by using a stretching function to reduce the number of grid points required for convergence (Sahu & Govindarajan 2016). However, in the present analysis, even in the absence of clustering, a satisfactory convergence has been achieved with 200 collocation points.

3.4.4. *Validation of numerical method*

In order to validate the results obtained from the numerical method, we draw a parallel between the EHD flow (abbreviated as EHDF) studied in the present report with the single fluid plane Poiseuille flow (abbreviated as SFPF), as described in Schmid & Henningson (2001) for $Re = 10\,000$. The consistency of the numerical method is checked by setting significantly lower values for V^L, representing a negligible viscosity gradient in the flow, so that the flow can be essentially considered

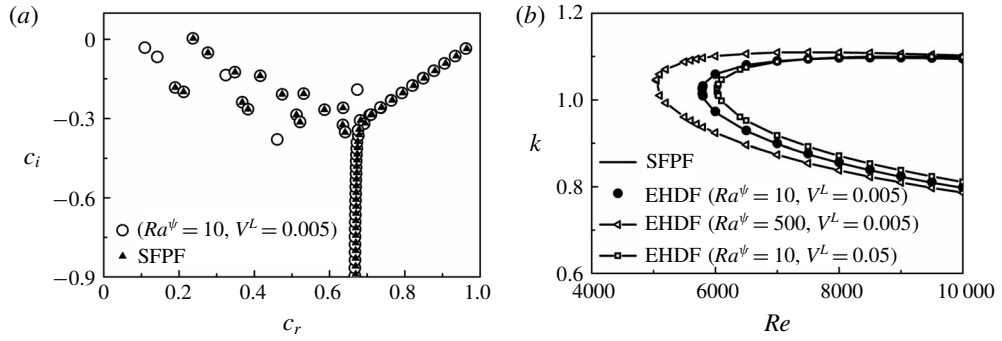

FIGURE 5. (*a*) Eigenspectra depicting the real part (c_r) versus imaginary part (c_i) of the complex wave speed c, for single fluid plane Poiseuille flow (SFPF) and EHD flow (EHDF) when $Re = 10\,000$ and $k = 1$, and (*b*) neutral stability curves showing the variation of k with Re for SFPF and EHDF. The other parameters considered for EHDF are $h = -0.3$, $\delta = 0.02$ and $Sc = 10$.

to be composed of a single fluid. The electric field force is turned off by assigning extremely low values to Ra^ψ. Hence, for imposed constraints of very low V^L and Ra^ψ, EHDF asymptotically emulates the SFPF. Figure 5 shows the eigenspectra and neutral stability plots for SFPF in tandem with the EHDF considered in the present analysis. Figure 5(*a*) shows the comparison between the eigenspectra depicting the imaginary part (c_i) versus the real part (c_r) of the complex wave speed, c, for the SFPF and the EHDF. The plot shows that, for a lower electric field potential ($Ra^\psi = 10$) and marginal viscosity difference ($V^L = 0.005$), the SFPF and EHDF generate similar eigenspectra. The latter produces a few extra eigenvalues owing to the marginal influence of the electric body force term in the momentum equation. Figure 5(*b*) depicts the neutral stability curves showing wavenumber (k) as a function of Reynolds number (Re) for SFPF and EHDF. For very low values of electric field and viscosity stratification ($Ra^\psi = 10$, $V^L = 0.005$), the EHDF shows a similar behaviour to the SFPF, yielding a critical Re of approximately 5772, as can be seen in figure 5(*b*). An increase in Ra^ψ signals an increment in the destabilizing electric field force, which is reflected as a decreasing trend of the critical Re with increasing Ra^ψ in figure 5(*b*). However, for a marginal increase in the viscosity difference between the fluids ($V^L = 0.05$) and for a lower electric field potential ($Ra^\psi = 10$), the critical Re for instability is found to increase, suggesting a kinetic stabilization of the system. Figure 5 shows the accuracy of the numerical analysis presented in this work, which has been employed to generate the results shown in the manuscript.

3.4.5. *Variable ionic mobility*

It may be noted here that, the ionic mobility parameter can strongly depend on the viscosity of the fluid (Schmidt & Yoshino 2015). Thus, it is likely that the ionic mobility values will differ in the fluids of interest in a practical setting. Although in the present analysis, for the purpose of mathematical simplification, most of the results are presented assuming equal ionic mobility, it is however lucrative to study the effect of a difference in the ionic mobility values in order to simulate a physical system with more precision. In order to investigate the effect of ion mobility values on the stability characteristics, we assume the ion mobility to be K_1 in the lower viscosity fluid 1 and K_2 in the higher viscosity fluid 2. The ionic mobility in the mixed interfacial is modelled as $K = K_1 \exp(SK^L)$, where S is the same scalar used for defining the

viscosity μ, and $K^L = \ln(K_2/K_1)$, is defined as the log mobility ratio. Subsequently, the perturbation scheme described by (3.19) becomes,

$$[u, w, p, \psi, S, \mu, K](x, z, t) = [u_0(z), 0, p_0, \psi_0(z), S_0(z), \mu_0(z), K_0(z)] + [\tilde{u}, \tilde{w}, \tilde{p}, \tilde{\psi}, \tilde{S}, \tilde{\mu}, \tilde{K}](z)\mathrm{e}^{(\omega t + \mathrm{i}kx)}. \tag{3.35}$$

The modified governing equation for the conservation of charge density q ((3.10) and (3.16)) can now be written as,

$$\frac{\partial q}{\partial t} + \boldsymbol{v} \cdot (\boldsymbol{\nabla} q) + Kq(\boldsymbol{\nabla} \cdot \boldsymbol{E}) + \boldsymbol{E} \cdot (K \boldsymbol{\nabla} q + q \boldsymbol{\nabla} K) = 0. \tag{3.36}$$

The base-state profile of the ionic mobility K_0 is obtained from the base-state solution of S_0 (3.20) as,

$$K_0 = \exp(S_0 K^L). \tag{3.37}$$

The base state of electric potential ψ_0 is obtained by solving the steady-state form of (3.36), given by,

$$K_0(\psi_0'')^2 + K_0 \psi_0' \psi_0''' + K_0' \psi_0' \psi_0'' = 0, \tag{3.38}$$

with the boundary conditions: $[\psi_0(1) = 1;\ \psi_0(-1) = 0;\ \psi_0''(1) = -I^q]$ as already mentioned previously. Upon perturbing the governing equations with the variables mentioned in (3.35), the modified dimensionless linearized charge conservation equation is given by,

$$\begin{aligned} \mathrm{i}k \left[(u_0 - c)(\tilde{\psi}'' - k^2 \tilde{\psi}) - \frac{\mathrm{i}}{k} \psi_0''' \tilde{w} \right] &= K_0 \psi_0' \tilde{\psi}''' + (2K_0 \psi_0'' + K_0' \psi_0') \tilde{\psi}'' \\ &+ (K_0 \psi_0''' + K_0' \psi_0'' - k^2 K_0 \psi_0') \tilde{\psi}' - (2k^2 K_0 \psi_0'' + k^2 K_0' \psi_0') \tilde{\psi} + \psi_0' \psi_0'' \tilde{K}' \\ &+ [(\psi_0'')^2 + \psi_0' \psi_0'''] \tilde{K}. \end{aligned} \tag{3.39}$$

The linearized non-dimensional governing equations defined by (3.24), (3.39) and (3.26) along with the boundary conditions defined by (3.27)–(3.29), are solved using the numerical method described in § 3.4.3.

3.4.6. *Variable dielectric constant*

As the case of ionic mobility, it is also quite likely that the experimental fluids seldom have similar dielectric constants. In order to investigate the effect of variable dielectric constants on the stability characteristics, we assume dielectric constants ε_1 and ε_2 for fluids 1 and 2, respectively. In the mixed interfacial region, the dielectric constant is modelled as $\varepsilon = \varepsilon_1 \exp(SE^L)$, where $E^L = \ln(\varepsilon_2/\varepsilon_1)$ is defined as the log permittivity ratio. The perturbation scheme shown in (3.19) transforms into,

$$[u, w, p, \psi, S, \mu, \varepsilon](x, z, t) = [u_0(z), 0, p_0, \psi_0(z), S_0(z), \mu_0(z), \varepsilon_0(z)] + [\tilde{u}, \tilde{w}, \tilde{p}, \tilde{\psi}, \tilde{S}, \tilde{\mu}, \tilde{\varepsilon}](z)\mathrm{e}^{(\omega t + \mathrm{i}kx)}. \tag{3.40}$$

The base-state profile of dielectric constant ε_0 is obtained from the base state of the concentration scalar S_0 as,

$$\varepsilon_0 = \exp(S_0 E^L). \tag{3.41}$$

The base-state electric potential ψ_0 is obtained by solving the steady-state form of (3.16), given by,

$$\varepsilon_0(\psi_0'')^2 + 3\varepsilon_0' \psi_0' \psi_0'' + \varepsilon_0 \psi_0' \psi_0''' + \varepsilon_0''(\psi_0')^2 = 0. \tag{3.42}$$

Equation (3.42) is solved using the boundary conditions: $[\psi_0(1) = 1;\ \psi_0(-1) = 0;\ \psi_0''(1) = -I^q]$. The modified dimensionless linearized momentum equation is given by,

$$\begin{aligned} &Re^{\psi}\mathrm{i}k[(u_0 - c)(\tilde{w}'' - k^2\tilde{w}) - u_0''\tilde{w}] \\ &\quad + Ra^{\psi}k^2[\varepsilon_0\psi_0'\tilde{\psi}'' - (\varepsilon_0\psi_0''' + k^2\varepsilon_0\psi_0' + 2\varepsilon_0'\psi_0'' + \varepsilon_0''\psi_0')\tilde{\psi} + (\psi_0')^2\tilde{\varepsilon}' + 2\psi_0'\psi_0''\tilde{\varepsilon}] \\ &= \mu_0\tilde{w}'''' + 2\mu_0'\tilde{w}''' + (\mu_0'' - 2k^2\mu_0)\tilde{w}'' - 2k^2\mu_0'\tilde{w}' + (k^2\mu_0'' + k^4\mu_0)\tilde{w} - \mathrm{i}ku_0'\tilde{\mu}'' \\ &\quad - 2\mathrm{i}ku_0''\tilde{\mu}' - (\mathrm{i}ku_0''' + \mathrm{i}k^3u_0')\tilde{\mu}. \end{aligned} \tag{3.43}$$

The linearized charge conservation equation is given by,

$$\begin{aligned} &\mathrm{i}k\left[(u_0 - c)(\varepsilon_0\tilde{\psi}'' + \varepsilon_0'\tilde{\psi}' - k^2\varepsilon_0\tilde{\psi} + \psi_0'\tilde{\varepsilon}' + \psi_0''\tilde{\varepsilon}) - \frac{\mathrm{i}}{k}(\varepsilon_0\psi_0''' + 2\varepsilon_0'\psi_0'' + \varepsilon_0''\psi_0')\tilde{w}\right] \\ &= \varepsilon_0\psi_0'\tilde{\psi}''' + (2\varepsilon_0\psi_0'' + 3\varepsilon_0'\psi_0')\tilde{\psi}'' + (\varepsilon_0\psi_0''' + 2\varepsilon_0''\psi_0' + 3\varepsilon_0'\psi_0'' - k^2\varepsilon_0\psi_0')\tilde{\psi}' \\ &\quad - (2k^2\varepsilon_0\psi_0'' + 2k^2\varepsilon_0'\psi_0')\tilde{\psi} + (\psi_0')^2\tilde{\varepsilon}'' + 3\psi_0'\psi_0''\tilde{\varepsilon}' + (\psi_0'\psi_0''' + \psi_0''^2)\tilde{\varepsilon}. \end{aligned} \tag{3.44}$$

Equations (3.43) and (3.44) along with (3.26) are solved using the boundary conditions mentioned in (3.27)–(3.29) applying the numerical method discussed in § 3.4.3.

3.5. *Nonlinear simulations*

The computational domain for the nonlinear simulations is shown in figure 3(*b*). The properties of the fluids are modelled as, $X = X_1\exp(SX^L)$, where X is a physical property (viscosity (μ_1, μ_2), dielectric constant (ε_1, ε_2) or ionic mobility (K_1, K_2)), S is any scalar and X^L is the log ratio. The governing equations simulated for the system are same as defined in § 3.2 ((3.2)–(3.11)).

For the flow field ((3.2) and (3.3)), a no-slip ($\boldsymbol{v} = 0$) condition was enforced at the walls. For the advection–diffusion equation (3.11), the inlet concentration was fixed at 1 for the higher viscosity (dielectric constant, ionic mobility) fluid and at 0 for the lower one. For the electric field (3.6), $\psi = \Psi_0$ and $\psi = 0$ boundary conditions were enforced at the top and bottom electrodes, respectively. The injection was considered autonomous and homogenous (refer to § 2.2). Thus, for the charge conservation equation defined by (3.7), constant charge density, $q = Q_0$, was maintained at the injector (top). It was also assumed that the ions discharged immediately on reaching the collector electrode (Wu *et al.* 2013, 2015).

The set of partial differential equations defined by (3.2)–(3.11) were solved using the finite element method employing the commercial software COMSOL Multiphysics™ for a 2-D geometry shown in figure 3(*b*). The domain was discretized with $\sim 4.5 \times 10^4$ finite elements with refinement along the walls, mixed interface and electrode regions. Second-order elements for velocity, concentration, potential and volume charge density, and first-order elements for pressure, were used for discretization. The MUltifrontal Massively Parallel Sparse direct solver (MUMPS) was used for solving the equations. The time dependent solver was adjusted to a backward difference formula with free time stepping for integrating the equations.

4. Results and discussion

4.1. *Experimental observations*

We initiate the discussion with one of the experimental results in which a benzene–silicone oil system ($V^L \approx 6$) flowed through a microchannel before the EHD field

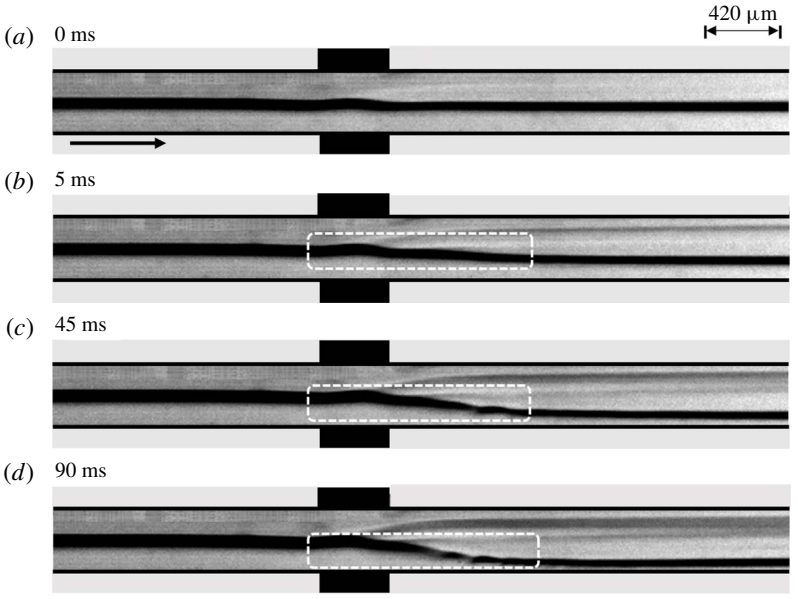

FIGURE 6. (*a–d*) Show the experimental snapshots after 0 ms, 5 ms, 45 ms and 90 ms, respectively, depicting the response of a stratified flow of a benzene–silicone oil system through the microchannel under an applied potential of 300 V ($Ra^{\psi} = 225$). Here, (*a*) corresponds to the system under 0 V electric potential. The top layer on the image corresponds to benzene and the bottom layer corresponds to silicone oil. The fluids flowed side by side in the channel while the images were taken from the top. The average *Re* of the base flow was maintained approximately at 0.5. The arrow indicates the direction of flow.

was generated by the application of a DC voltage of 300 V ($Ra^{\psi} = 225$) across the electrodes. Figure 6 shows the images of the experiment, which correspond to the top view of the flow while the electrodes were inserted into the channel horizontally from the sides, as previously mentioned in figure 1. The supporting movie 1 available at https://doi.org/10.1017/jfm.2018.1023 shows the spatio-temporal evolution of the instability near the electrode with the finer details. The experiments were visualized using a microscope under 2.5× magnification and recorded using a high speed camera at 500 fps at a resolution of 1280 × 120 pixels unless stated otherwise. It may be noted here that a higher difference in the viscosities of benzene and silicone oil helped us in capturing the high quality grey scale videos, as reported here. The EHD instability phenomenon was reproducible for benzene–oleic acid and benzene–soybean oil systems too. However, those results are not reported for the sake of brevity. Figure 6(*a*) shows that the pressure-driven flow rates of the fluids were attuned in such a manner that a steady stratified flow was formed in the absence of the external field. Figure 6(*b–d*) and the supporting movie 1 show the typical evolution of the miscible benzene–silicone oil interface under the influence of the electric field. It may be noted here that the top layer shown in the image is benzene while the bottom one is silicone oil. However, in reality, the fluids flowed side by side in the channel while the images were taken from the top. On application of the electric field potential through the electrodes, the flow becomes unstable and develops instabilities, as shown with the help of highlighted rectangular boxes in the

images. The images and the video suggest that the applied field destabilizes the lower viscosity benzene layer and subsequently shifts the diffused interface towards the more viscous silicone oil layer. Under the exposure of a constant electric field intensity, the instability possesses convective waves propagating towards the downstream of the channel owing to the presence of the pressure-driven flow inside the channel. After the onset, the speed of these waves increase with time before reaching a constant value for given field intensity, as shown in figure 6(*b–d*) and the supporting movie 1.

4.2. *Theoretical outlook of the instabilities*

The details of the theoretical formulation are deliberated in § 3 while the results obtained from the LSA are discussed in this section. We have identified that, for the proposed system, the effects of Ra^{ψ}, V^L and Sc are perhaps the most significant ones because all of the different modes of instability pertaining to this system are obtained with variations in the magnitudes of these parameters. The results (except for figures 13–15) correspond to $K_L = 0$ and $E_L = 0$, unless otherwise stated. Figure 7(*a*) depicts the neutral stability plot showing the variation of the wavenumber (k) with Ra^{ψ} for $V^L = 1$. The plot suggests that the system is unstable to a finite-wavenumber mode of instability at low and intermediate values of Ra^{ψ} (solid line). We term this mode the electric field mode I (E-I). At higher values of Ra^{ψ} the system becomes unstable to another finite-wavenumber mode of instability (broken line) termed the electric field mode II (E-II). The wave speed (c_r) of the E-I-mode is found to match with the theoretical average velocity (u_0) of the lower viscosity fluid (fluid 1) whereas the wave speed of the E-II-mode matches with the mean flow of the higher viscosity fluid (fluid 2). This observation helps in inferring that the EHD field can destabilize the lower viscosity fluid at much lower values of Ra^{ψ} to manifest the E-I-mode while the E-II-mode appears at a much higher value of Ra^{ψ} in the higher viscosity fluid 2. The typical ω versus k plots with the variation in Ra^{ψ} are shown in figure 7(*d*). At $Ra^{\psi} = 400$, only E-I-mode exists (unevenly broken line) whereas at $Ra^{\psi} = 1125$, both E-I and E-II modes (triangular symbols) are present with the E-I-mode characterized by significantly higher growth rates than the E-II-mode. Figure 7(*b*) illustrates the variation of wavenumber against log viscosity ratio (V^L) for $Ra^{\psi} = 375$. The plot suggests that, at lower values of V^L, only the E-I-mode (solid line) can destabilize the flow. In comparison, at higher values of V^L, a much longer-wavelength viscous mode (V) (unevenly broken line) appears alongside the E-I-mode. At the intermediate values of V^L, ranging from 1.3 to 1.6, a unique bimodal behaviour is observed, as shown by the ω versus k plots in figure 7(*e*). The plots clearly suggest that the V-mode arises only when there is a higher viscosity contrast across the diffused interface. Figure 7(*c*) shows the variation of k with Sc for $V^L = 2$ and $Ra^{\psi} = 375$. In this situation, apart from the E-I mode (solid line), the diffusive D-mode becomes unstable beyond a threshold value of Sc. The D-mode exhibits a finite-wavenumber-type behaviour for low to intermediate values of Sc, which signifies a thick and diffusive interface. At higher values of Sc, when the interface is much sharper and thinner, the D-mode behaves as a long-wave mode, frequently observed for immiscible two-phase flows (Ern *et al.* 2003; Sahu & Govindarajan 2016). The ω versus k plots in figure 7(*f*) shows the transition of the length scale from the shorter- to longer-wavelength regime with the increase in Sc.

In summary, figure 7 uncovers four distinctive finite-wavenumber modes destabilizing a two-layer viscosity stratified flow of miscible fluids under the influence of an externally applied electric field. The results suggest the existence of two distinct

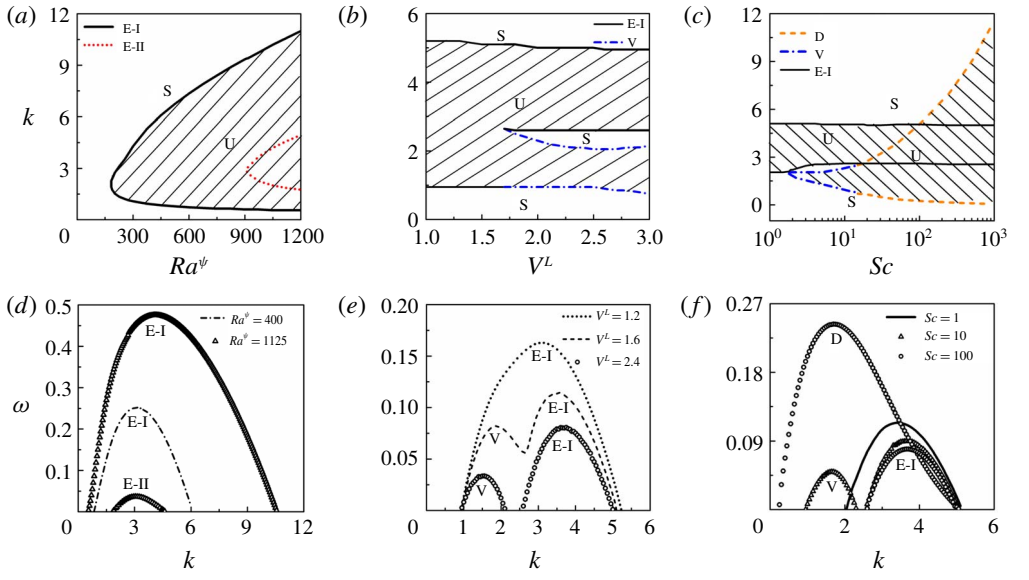

FIGURE 7. (Colour online) Neutral stability plots showing the variations of wavenumber (k) with (a) electric Rayleigh number Ra^{ψ}, (b) log viscosity ratio V^L and (c) Schmidt number Sc. The dispersion curves showing the growth rate (ω) versus the wavenumber (k) of the unstable modes with (d) Ra^{ψ}, (e) V^L and (f) Sc. In (a) the solid line represents the electric field mode I (E-I) and the broken line represents the electric field mode II (E-II). The other parameters for (a,d) are $V^L = 1$, $h = -0.3$, $\delta = 0.02$, $Sc = 10$ and $Re = 0.5$. In (b) the solid lines represent electric field mode I (E-I) and the unevenly broken lines represent the viscous mode (V). The other parameters for (b,e) are $h = -0.3$, $\delta = 0.02$, $Sc = 10$, $Ra^{\psi} = 375$ and $Re = 0.5$. In (c) the solid lines represent the E-I-mode, the unevenly broken line represents the V-mode and the evenly broken line denotes the diffusive mode (D). The other parameters for (c,f) are $V^L = 2$, $h = -0.3$, $\delta = 0.02$, $Ra^{\psi} = 375$ and $Re = 0.5$. The hatched U-regions denote unstable zones whereas S-regions denote the stable zones.

electric field modes, E-I and E-II, beyond a critical value of Ra^{ψ}. Further, the presence of the V- and D-modes are also observed due to the viscosity stratification and convective transport of the perturbed concentration near the interface, respectively.

In order to evaluate the contributions of the various forces to the growth of the instability modes discussed above, an energy analysis is carried out. A brief outline of the analysis is provided in appendix A. The energy equation relates the rate of change of the disturbance kinetic energy (E_{KE}), with energy changes associated with the Reynolds stress (E_{RS}), viscous dissipation (E_{VD}), viscosity stratification (E_V) and electric force (E_E) components. Figure 8 describes the variation of the normalized energy associated with the various terms (E_N) with Ra^{ψ}, V^L and Sc. It may be noted here that the eigenfunctions used for the energy calculations correspond to those of the most unstable modes. Further, the eigenfunctions are normalized with their maximum absolute values while the energy terms are normalized by the total kinetic energy $\int_{-1}^{1}(|\tilde{u}|^2 + |\tilde{w}|^2)\,\mathrm{d}z$. The variation of E_{RS} is not shown in the plots because the energy associated with the Reynolds stresses are negligible for the flows with low Re reported in this work.

Figure 8(a) shows that, for the situation with a lower viscosity stratification ($V^L = 1$), the major part of the disturbance energy is generated by the applied electric force,

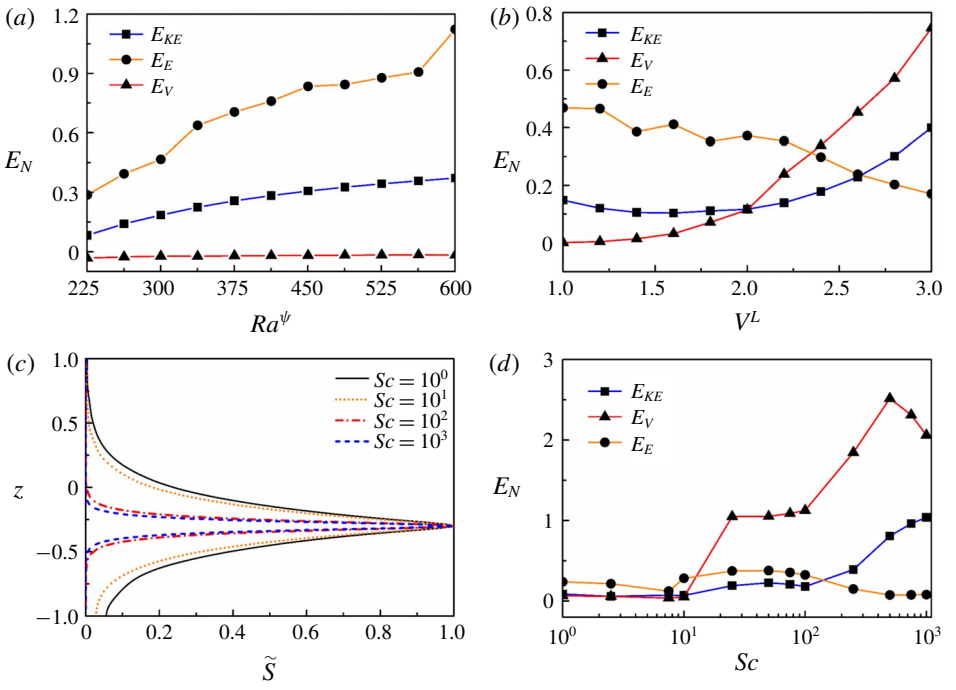

FIGURE 8. (Colour online) The variations of (*a*) normalized energy (E_N) with Ra^{ψ}, (*b*) normalized energy with V^L, (*c*) absolute values of normalized perturbation concentration ($\tilde{S}$) with Sc and (*d*) normalized energy with Sc. The other parameters for (*a*) are $V^L = 1$, $h = -0.7$, $\delta = 0.02$, $Sc = 10$ and $Re = 0.5$. The other parameters for (*b*) are $h = -0.3$, $\delta = 0.02$, $Sc = 10$, $Ra^{\psi} = 375$ and $Re = 0.5$. The other parameters for (*c*,*d*) are $V^L = 3$, $h = -0.3$, $\delta = 0.02$, $Ra^{\psi} = 375$ and $Re = 0.5$.

which is reflected in the higher values of E_E. With the increase in electric force (Ra^{ψ}), E_E increases monotonically, which is the cause of the onset of the E-I and E-II modes. In this case, the energy associated with viscosity stratification (E_V) is negligible, and remains nearly unchanged with increment in Ra^{ψ}. The trends of the variation in E_E and E_V with Ra^{ψ} explain well the occurrence of the electric field modes at lower viscosity stratifications, as previously discussed with figure 7(*a*,*d*). Figure 8(*b*) depicts the variations of E_N with V^L, which reveals that the electric force remains the major source of disturbance at lower values of V^L. Hence, for lower viscosity stratifications, only the E-I-mode of instability manifests in the system, as depicted in figure 7(*b*,*e*). With the increase in V^L, the energy associated with viscosity stratification increases rapidly, leading to the occurrence of the V-mode of instability along with the E-I-mode. Figure 8(*c*) shows the variation of the absolute values of the normalized perturbation concentration ($\tilde{S}$) for different values of Sc. At lower values of Sc the variation in $\tilde{S}$ is found to be progressive and less steep near the mixed interface. The variation in $\tilde{S}$ becomes steeper across the interface at higher values of Sc, which gives rise to the onset of the D-mode of instability. Figure 8(*d*) shows the variation of E_N with Sc. The plot suggests that at lower values of Sc, the disturbance kinetic energy is produced mainly by the applied electric force, which is indicated by the higher values of E_E. At higher values of Sc, E_V contributes more towards the

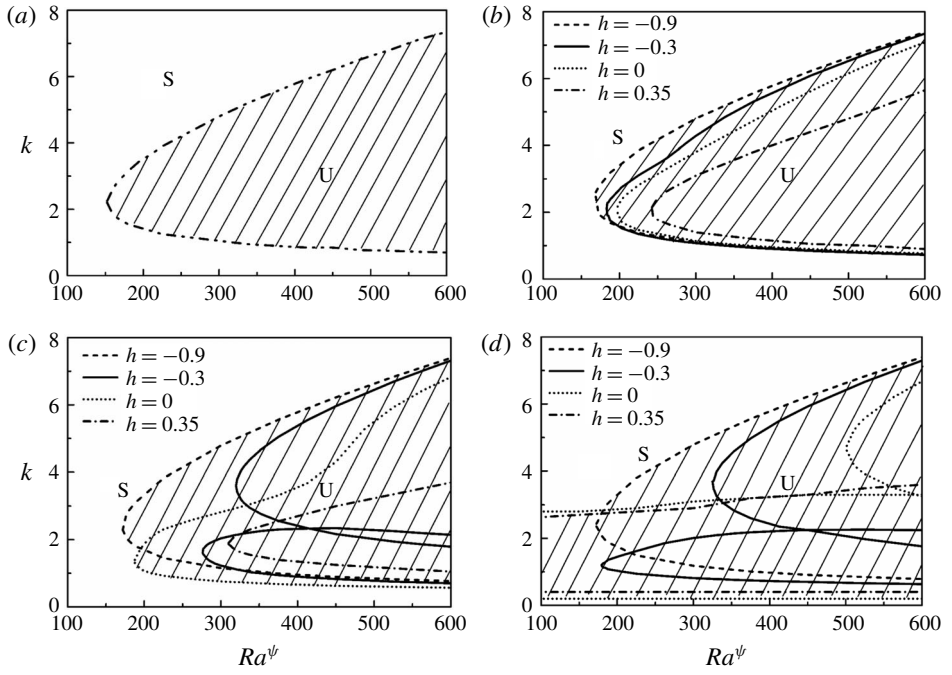

FIGURE 9. Neutral stability plots showing the variation of wavenumber (k) versus electric field Rayleigh number (Ra^{ψ}) for (*a*) $V^L = 0$, (*b*) $V^L = 1$, (*c*) $V^L = 2$ and (*d*) $V^L = 3$. In (*b–d*) the evenly broken, solid, dotted and unevenly broken lines show the situations with $h = -0.9, -0.3, 0$ and 0.35, respectively. The other parameters are $Sc = 10$, $\delta = 0.02$ and $Re = 0.5$. The hatched U-regions denote unstable zones whereas S-regions denote the stable zones.

generation of disturbance energy compared to E_E, which causes the D-mode to occur alongside the E-I-mode, as previously observed in figure 7(*c*,*f*).

4.2.1. *Parametric study*

In this section we discuss the role of various parameters in influencing the stability of the system. Figure 9(*b*) shows the variation of k with Ra^{ψ} for different values of h, which signifies the distance of the diffused interface from the datum, $z = 0$, as previously shown in figure 3(*a*). It may be noted here that the variation of h from -1 to 1 also signifies the progressive filling of the channel with a more viscous fluid. Figure 9(*a*) shows the situation when $V^L = 0$, which indicates that the channel is entirely filled with the low viscosity fluid. The plot shows that the system is unstable to the E-I-mode of instability. In figure 9(*b–d*) the evenly broken, solid, dotted and unevenly broken lines show the situations with $h = -0.9$, -0.3, 0 and 0.35, respectively, which signify that the channel is filled with thin (e.g. $h = -0.9$) to thick (e.g. $h = 0.35$) layers of more viscous fluid in the fully developed stratified flow.

Figure 9(*b*) shows the neutral stability curves when $V^L = 1$, for different values of h. The plot suggests that as the proportion of the more viscous fluid increases inside the channel, the critical Ra^{ψ} for the E-I-mode progressively increases owing to the increase in the overall viscous resistance. The neutral stability curves in figure 9(*c*) for

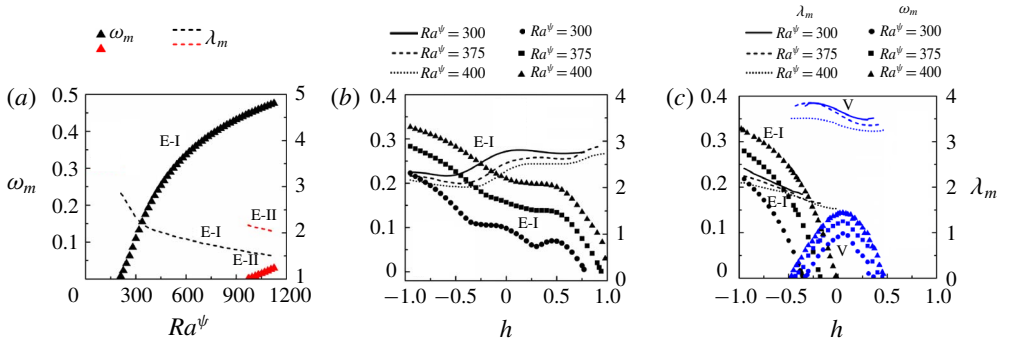

FIGURE 10. (Colour online) (*a*) Shows the variations of dominant growth rate (ω_m, denoted by symbols) and wavelength (λ_m, denoted by lines) with Ra^{ψ}. (*b*,*c*) Show the variations of dominant growth rate (ω_m, denoted by symbols) and wavelength (λ_m, denoted by lines) with h, at different values of Ra^{ψ} for $V^L = 1$ and $V^L = 2$, respectively. The other parameters considered for (*a*) are $V^L = 1$, $h = -0.3$, $\delta = 0.02$, $Sc = 10$ and $Re = 0.5$. The other parameters considered for (*b*,*c*) are $h = -0.3$, $\delta = 0.02$, $Sc = 10$ and $Re = 0.5$.

$V^L = 2$ show the presence of the E-I-mode for the situations with a thinner layer of more viscous fluid. The plot shows the appearance of the twin E-I and V modes with shorter and longer wavelengths, respectively, as the thickness of the layer with more viscosity is increased at $h = -0.3$. The V-mode arises due to the viscosity stratification across the diffused interface, while the origin of the E-I-mode can be attributed to the externally applied electric field, as discussed previously. Notably, the E-I-mode is found to have a much shorter wavelength, compared to the V-mode. The V-mode becomes unstable at a much lower value of Ra^{ψ} when the thickness of the more and less viscous fluids are identical at $h = 0$. With further increase in the thickness of the higher viscosity fluid, the increase in the viscous resistance inside the channel enforces the V-mode to appear at a higher value of Ra^{ψ} for $h = 0.35$. Again, the E-I-mode for this plot appears at a much higher value of Ra^{ψ}, which is not shown. Figure 9(*d*) shows the results for $V^L = 3$, which are very similar in nature to those observed in figure 9(*c*). However, for $V^L = 3$, the V-mode becomes unstable even in the absence of an externally applied electric field beyond a certain value of h, as can be seen for $h = 0$ and $h = 0.35$. Thus, the V-mode is found to have similar characteristics to the shear mode of instability in the viscosity stratified flow of miscible fluids, which has been reported in previous works (Talon & Meiburg 2011).

Figure 10(*a*) depicts the variations of the dominant growth rate (ω_m) and wavelength (λ_m) representing the most unstable disturbances with Ra^{ψ} for $V^L = 1$. The plot suggests that, for low and intermediate values of Ra^{ψ}, the system manifests the E-I-mode (black symbols) whereas at higher values of field intensity the E-II-mode (red symbols) appears along with the E-I-mode. Figure 10(*b*) shows the variations of ω_m and λ_m with h across the channel for three different values of Ra^{ψ}. Again, in this plot the variation of h from -1 to 1 signifies the progressive filling of the channel with the more viscous fluid. The plot suggests that when $V^L = 1$, the E-I-mode progressively loses its strength (ω_m reduces) when the channel is filled with the more viscous fluid provided Ra^{ψ} is kept constant. Subsequently, a marginal increase in λ_m of the E-I-mode is also observed. The plot also shows that the time and length scales of the E-I-mode reduce with the increase in Ra^{ψ} because the magnitude of ω_m increases and λ_m reduces with the increase in Ra^{ψ}. In comparison, figure 10(*c*)

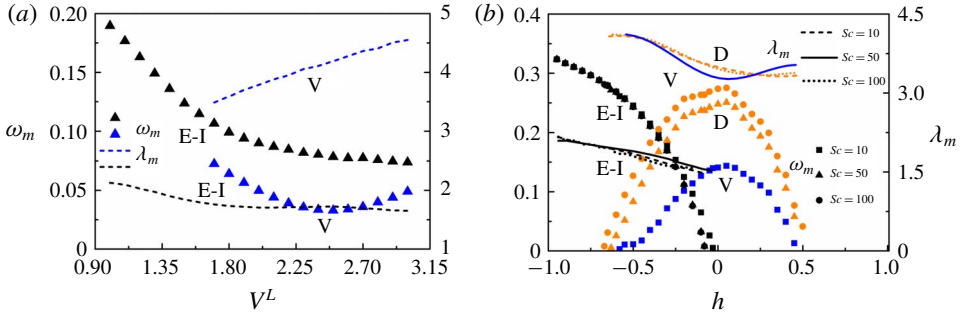

FIGURE 11. (Colour online) (*a*) Shows the variations of dominant growth rate (ω_m, denoted by symbols), and wavelength (λ_m, denoted by lines) with V^L. The other parameters considered are $h = -0.3$, $\delta = 0.02$, $Sc = 10$, $Ra^{\psi} = 375$ and $Re = 0.5$. (*b*) Shows the variations of dominant growth rate (ω_m, denoted by symbols) and wavelength (λ_m, denoted by lines) with h for different values of Sc. The other parameters are, $V^L = 2$, $\delta = 0.02$, $Ra^{\psi} = 375$ and $Re = 0.5$.

shows that, for higher values of $V^L (V^L = 2)$, the E-I-mode is the dominant one at lower values of h. However, the reduction in ω_m of the E-I-mode happens at a much faster rate with the increase in h while a subdominant V-mode appears due to the combined influence of electric field and viscosity stratification at intermediate values of h. At even higher values of h, the E-I-mode disappears, and the V-mode becomes the dominant mode. Interestingly, at intermediate values of h both the modes co-exist to engender a bimodal instability. The plot suggests that the time and length scales of both the E-I-mode and V-mode reduce with the increase in Ra^{ψ} because the magnitude of ω_m increases and λ_m reduces with the increase in Ra^{ψ} as previously observed in the case of $V^L = 1$. Thus, an externally applied electric field can stimulate both the finite-wavenumber E-I and V modes at lower Re of the stratified flow of miscible fluids.

Another important parameter, which strongly influences the nature of the instabilities in the present setting, is the viscosity contrast between the fluids defined by log viscosity ratio V^L. Figure 11(*a*) shows the variations of ω_m and λ_m with V^L. The plot suggests that when the viscosity contrast across the diffused interface is lower, the E-I-mode is the dominant one whereas, with a progressive increase in V^L, the V-mode can become the dominant one (not shown here). The plot also shows a much smaller length scale of the E-I-mode as compared to the V-mode. It is important to note here that Sc is another crucial parameter for defining the stability of miscible flows. The effect of Sc on various configurations of miscible flows have been discussed in detail in previous literature (Sahu & Govindarajan 2016). However, the presence of an electric field in this regard makes the study more interesting. It has been discussed earlier that the Sc number contributes to the appearance of the D-mode beyond a critical threshold. Figure 11(*b*) shows the variation of ω_m and λ_m with h for three different values of Sc. It can be inferred from the figure that the E-I-mode remains almost unaffected by the increase in Sc. However, as the interface becomes thinner and less diffusive (higher Sc, filled circular and triangular symbols) the V-mode which occurs at $Sc = 10$ undergoes transition to the D-mode which is accompanied by a drastic increase in the growth rates of the most unstable perturbations. At higher values of h, again the increase in the viscous resistance owing to the presence of the more viscous liquid reduces the growth rate of the D-mode.

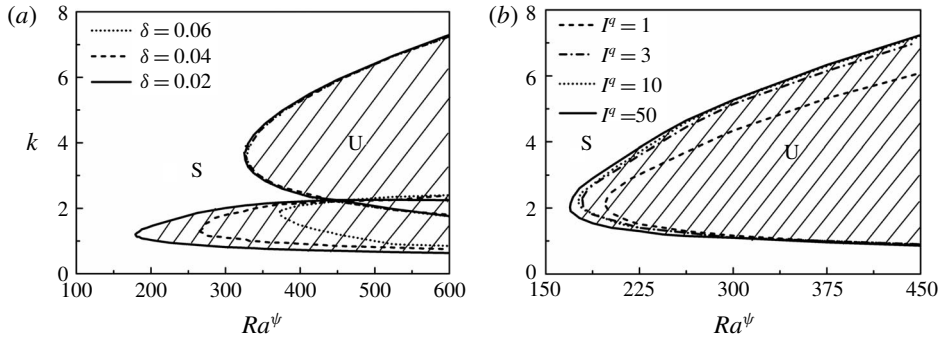

FIGURE 12. Neutral stability plots showing the variation of k with Ra^{ψ} for (a) different values of thickness of the mixed interface, δ, and (b) different values of the injection level I^q. The other parameters for (a) are $V^L = 2$, $h = -0.3$, $Sc = 10$ and $Re = 0.5$ and for (b) are $V^L = 1$, $h = -0.3$, $\delta = 0.02$, $Sc = 10$ and $Re = 0.5$. The hatched U-regions denote unstable zones whereas S-regions denote the stable zones.

It is now well understood that the thickness of the mixed interface plays a significant role in determining the stability characteristics of the system (Talon & Meiburg 2011). While a thicker mixed interface damps a perturbation due to molecular diffusion, a thin interface with restricted diffusion makes a perturbation unstable owing to steep viscosity profiles near the interfacial region. The neutral stability plot shown in figure 12(a) describes the effect of δ on the stability behaviour for $V^L = 2$. While the E-I-mode remains unaffected by δ, the V-mode exhibits profound stabilization with an increase in δ. Apart from the interfacial thickness, the level of charge injection, I^q, can also influence the critical conditions of the E-I-mode. Figure 12(b) shows that the critical Ra^{ψ} reduces significantly with the increase in I^q. This observation is in qualitative agreement with the results of Zhang *et al.* (2015) for a single fluid.

The difference in ionic mobility in the two fluids can be a critical parameter in governing the stability characteristics of the system under study. The base-state profile for electric potential ψ_0 is shown in figure 13 for different values of K^L. The variation of ionic mobility across the channel is consequential in the distribution electric potential across the channel. In the case of uniform mobility across the channel ($K^L = 0$), the base-state profile of electric potential is progressive, as shown in figure 13. However, with a decrease in the value of ionic mobility in the higher viscosity fluid, there is a build-up of charge in the mixed interfacial region, which is depicted by the cusps in the profiles of the electric potential ψ_0 near the mixed interfacial region for $K^L = -2$, $K^L = -3$ and $K^L = -4$. Figure 14(a) depicts the neutral stability plots for different values of K^L, at $V^L = 1$ and $h = -0.7$. It can be inferred from the plot that, as the mobility values decrease in the higher viscosity fluid, the critical electric field needed to trigger the E-I-mode of instability increases. However, with an increase in the proportion of the more viscous fluid ($h = -0.3$), there is a substantial increase in the growth rates (ω_m) at $K^L = -3$ and $K^L = -4$, compared to $K^L = 0$ as seen from figure 14(b,c). The instabilities also exhibit much shorter wavelengths compared to the finite-wavenumber E-I-mode of instability. We hereafter refer to this mode as the K-mode of instability. Figure 14(d) shows the variation of ω_m with the location of the mixed layer (h). It can be inferred from the plot that, for greater proportions of less viscous (higher mobility) fluid inside the channel, the system becomes unstable to the E-I-mode of instability (triangular symbols). The

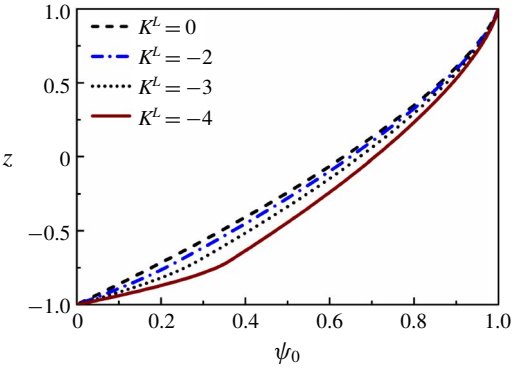

FIGURE 13. (Colour online) Base-state profile for electric potential (ψ_0) for different values of log mobility ratio K^L. The other parameters are $h = -0.3$ and $\delta = 0.02$.

interface is located close to the walls when the proportion of either fluid is very high inside the channel. Thus, any perturbation occurring within the interfacial region due to difference in ionic mobility is stabilized by viscous dissipation. Thus, only the E-I-mode occurs for high proportions of the less viscous fluid inside the channel. With an increase in the proportion of the more viscous (lesser mobility) fluid, as the location of the interface h shifts towards the centre of the channel, the instability is governed by the K-mode with higher growth rates and lower wavelength as compared to the E-I-mode. The K-mode occurs in the mixed interfacial region due the steep gradient in charge density in the region caused by the difference in ionic mobility between the fluids. Again, it can be seen from figure 14(*e*,*f*) that, for higher viscosity stratification, the stability characteristics change on varying the ionic mobility of the fluids. For $K^L = -4$, as depicted by figure 14(*f*), only the K-mode of instability exists, unlike the V-mode and the E-I-mode depicted in figure 14(*e*) for $K^L = 0$. It may be noted that with a further increase in viscosity stratification, the V-mode also occurs in conjunction with the K-mode (not shown here).

The dielectric constant is another important parameter that can be consequential to the stability characteristics of the system under study. Figure 15 shows the neutral stability curves depicting the variation of k with Ra^{ψ} for different values of E^L. The plot predicts an increase in the critical values of Ra^{ψ} with an increase in the permittivity stratification inside the channel compared to the case of uniform permittivity ($E^L = 0$). It may be noted here that, in this work, the higher permittivity is used as the characteristic permittivity. Hence, negative (positive) sign in the value of E^L signifies that the permittivity of fluid 2 is lesser (higher) than that of fluid 1. It can be inferred from figure 15 that, for slight differences in the values of electric permittivity of the two fluids, the critical conditions for the onset of the instabilities remain very close to each other. Significant changes in the onset conditions are only observed for larger differences in the values of dielectric constants of the two fluids. Since this study is motivated by fluids with similar dielectric constants, we do not undertake an in-depth analysis of the consequences of larger contrasts in the dielectric constants.

Figures 7–15 together provide some clue to the onset of instability in a two-layer viscosity stratified flow of miscible fluids, which has been observed in the experiment shown in figure 6. The plots reveal that the E-I-mode may appear even at very low flow rates beyond a critical electric field intensity, which suggests that the proposed

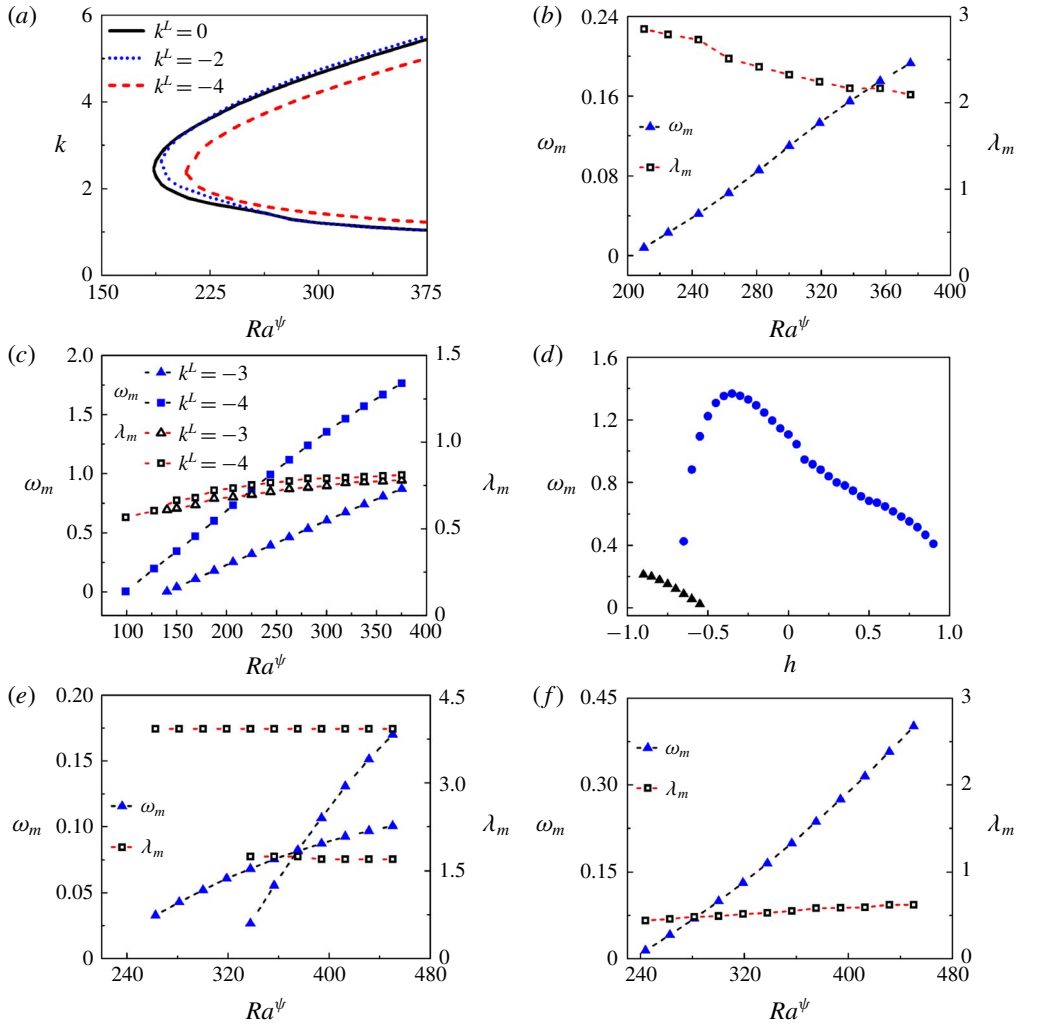

FIGURE 14. (Colour online) (*a*) Neutral stability curves showing the variation of wavenumber (k) with electric Rayleigh number (Ra^ψ) for different values of K^L. The other parameters are $V^L = 1$, $h = -0.7$, $\delta = 0.02$, $Sc = 10$ and $Re = 0.5$. Variation of the growth rate of the most unstable modes (ω_m) with Ra^ψ for (*b*) $K^L = 0$, (*c*) $K^L = -3$ and $K^L = -4$. The other parameters used for (*b*,*c*) are $V^L = 1$, $h = -0.3$, $\delta = 0.02$, $Sc = 10$ and $Re = 0.5$. (*d*) Variation of the growth rate of the most unstable modes (ω_m) for different values of h. The other parameters used are $V^L = 1$, $K^L = -4$, $Ra^\psi = 300$, $\delta = 0.02$, $Sc = 10$ and $Re = 0.5$. Variation of the growth rate of the most unstable modes (ω_m) with Ra^ψ for $V^L = 2$ and (*e*) $K^L = 0$ and (*f*) $K^L = -4$. The other parameters are $h = -0.3$, $\delta = 0.02$, $Sc = 10$ and $Re = 0.5$.

methodology can cause micromixing in the low Re flows. The threshold field intensity to instigate the instability can be reduced further by increasing the charge injection level, reducing the diffusion across the interface, and reducing the proportion of more viscous fluid. Further, both the layers can be made unstable at higher field intensities by simultaneously stimulating both the E-I and E-II modes. Conditionally, the V-mode

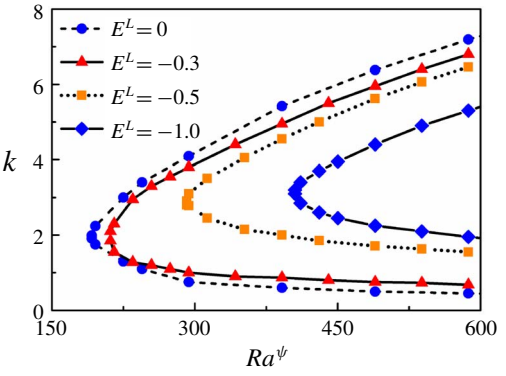

FIGURE 15. (Colour online) Neutral stability curves showing the variation of wavenumber (k) with electric Rayleigh number (Ra^ψ) for different values of E^L. The other parameters are $V^L = 1$, $K^L = 0$, $h = -0.3$, $\delta = 0.02$, $Sc = 10$ and $Re = 0.5$.

and D-modes may appear owing to the viscosity contrast across the interface and the convective transport at the diffused interface. A contrast in the ionic mobilities in the two fluids may also cause the appearance of the K-mode of instability characterized by higher growth rates compared to the E-I-mode. For small values of E^L, the nature and onset conditions of the instabilities are similar to the case of uniform dielectric constants.

4.3. *A comparison between experimental and theoretical results*

In this section, a comparison between the data obtained from the experiments, LSA and numerical simulations is reported. Here, we particularly focus on the critical voltage required to initiate the instability in the two-layer stratified flow of miscible fluids. Due to limitations in measurement techniques, the values of h and δ used for the theoretical calculations are assumed to emulate the experimental conditions closely. The precise calculation of the thickness of the mixed layer, δ, for a dynamic interface developed inside a microchannel is challenging. Further, the characterizations of such a diffuse interface between miscible fluids require sophisticated techniques, and are thus not attempted. In such a scenario, the value of δ was not measured directly from the experiments, but rather approximated with a simple order-of-magnitude analysis and CFD simulations, the details of which are provided in appendix C. The three experimental values denote benzene–oleic acid ($V^L \approx 3$), benzene–soybean oil ($V^L \approx 4$) and benzene–silicone oil ($V^L \approx 6$) fluid pairs. Figure 16 shows that the LSA over-predicts the corresponding experimental and simulation values. This is expected since the nonlinearity associated with the actual experimental phenomena is not considered in the LSA. In addition, the other parameters, such as the location of the mixed layer (h), thickness of the mixed layer (δ), the value of Sc, are set, for the LSA, to tentatively emulate the experimental conditions, as the measurement of these quantities is exceedingly challenging in the reported experimental set-up. Variation in the ionic mobilities and dielectric constants of the fluids, which are not considered in the LSA, can also be instrumental in determining the onset conditions, as hinted at in figures 14 and 15. In the absence of exact experimentally measured values of the ionic mobility and dielectric constant, the LSA was carried out considering equal ionic mobilities and dielectric constants for the fluids. Further, the injection of

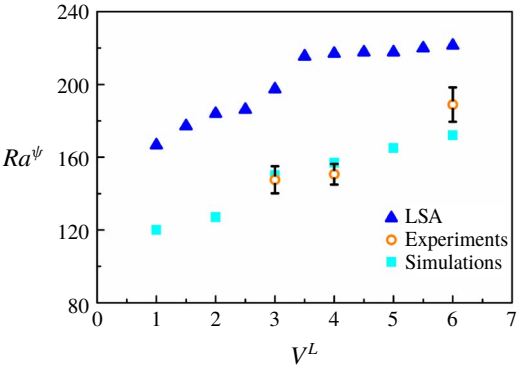

FIGURE 16. (Colour online) Variation of Ra^{ψ} with V^L depicted by LSA, experiments and numerical simulations. The other parameters used for LSA are $h = -0.6$, $\delta = 0.04$, $K^L = 0$, $E^L = 0$, $Sc = 500$ and $Re = 0.5$. The other parameters used for simulations are $K^L = 0$, $E^L = 0$, $Sc = 500$ and $Re = 0.5$. The experimental values denote benzene–oleic acid ($V^L = 3$), benzene–soybean oil ($V^L = 4$) and benzene–silicone oil ($V^L = 6$) fluid pairs. The average Re maintained during the experiments was 0.5. The error bars represent the standard deviations of three experiments.

charges from the electrodes is considered to be autonomous. However, it has been shown in earlier literature (Pontiga *et al.* 1995) that, for moderate injection levels, a realistic field-dependent injection law can yield results different from those of the autonomous injection case. Nevertheless, it can be seen that there is a reasonable qualitative agreement between the onset conditions obtained from the theory and the experiments. It is anticipated that, various assumptions made for the purpose of simplification of the mathematical model, when addressed accurately, would yield better agreement between the experimental and theoretical predictions.

Figure 17(*a*) shows experimental snapshots of the top view of the instabilities of a benzene–silicone oil system at different time intervals when exposed to an electric field potential of 400 V ($\boldsymbol{E} = 9.5$ kV cm^{-1}). Again, it may be noted here that the top layer shown in the image is benzene while the bottom one is silicone oil. However, in reality, the fluids flowed side by side while the images were taken from the top. The images show the progressive linear undulations near the interface and subsequent travelling waves towards the downstream of the channel under exposure to the electric field. Figure 17(*b*) shows a comparison between the theoretically calculated wavelengths (λ) and wave speeds (c_r), and their corresponding experimental values. In order to experimentally measure the wavelength and wave speed of the unstable waves, the system was subjected to DC electric fields before the response was recorded. The frames extracted from the videos were then analysed to measure the required quantities. The wave speed was measured by tracking a wave over a particular distance towards the downstream, and then estimating the time required for the motion, as shown by the boxes in figure 17(*a*).

The experimental wavelength and wave speed were compared with the wavelength and speed of the E-I-mode obtained from linear stability analysis. It can be seen from figure 17(*b*) that the experimental and theoretical wavelengths are of the order of $\sim 10^{-2}$ cm, while the wave speeds are found to be of the order of $\sim 10^{-1}$ cm s^{-1}. The plot also shows that the wavelengths obtained from the experimental and theoretical analyses show the same qualitative decreasing trend, whereas the wave speeds exhibit

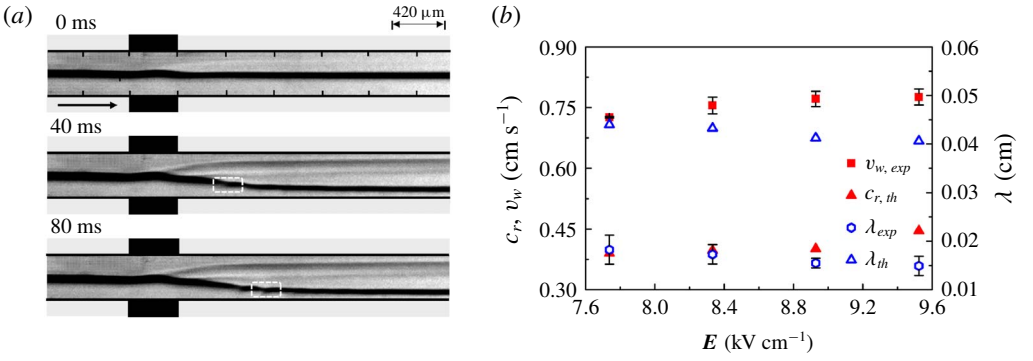

FIGURE 17. (Colour online) (*a*) Shows the experimental snapshots of a silicone oil–benzene system under application of an electric field of 9.5 kV cm^{-1} at different time instances. (*b*) Demonstrates the variation of experimental and theoretical wave speeds (v_w, c_r) and wavelengths (λ) with increasing electric field intensity ($\boldsymbol{E}$). The hollow symbols (blue) denote the values of the wavelengths, whereas the solid symbols (red) denote the wave speeds. The theoretical parameters used for the plot are $h = -0.6$, $\delta = 0.02$, $Sc = 500$ and $V^L = 6$. The error bars in the experimental points are twice the standard deviations obtained from three experiments. The average Re maintained during the experiments was 0.5. (*a*) Corresponds to the top view of the flow configuration. In the image the top (bottom) layer corresponds to benzene (silicone oil) while in reality they flowed side by side. The videos were recorded at 500 fps under 2.5× magnification. The arrow in (*a*) indicates the direction of the flow.

an increasing trend, with an increase in the strength of the applied electric field. Again, the plot shows that the experimentally observed quantities are slightly different from the values predicted theoretically, which can be attributed to the various factors mentioned previously.

4.4. *Experimental and simulation results: nonlinear, time-periodic and unsteady regimes*

Apart from the unstable linear modes, the experiments also uncovered the presence of interesting nonlinear, time-periodic and unsteady regimes in the two-layer stratified flow of miscible fluids under the influence of external EHD field inside a microchannel. In this section, we investigate the various flow patterns obtained during electroconvection when the applied field intensity is on the higher side. Upon application of electric potential to the system after development of a steady flow profile, four distinctive disturbance patterns are observed in the system, as demonstrated in figure 18. The image sets in figure 18(*a–d*) qualitatively identify these instability regimes, labelled as I, II, III and IV, as observed upon application of electric field from 0 to 35 kV cm^{-1}. In these images the layer shown at the top (bottom) corresponds to benzene (silicone oil). In these experiments, the voltage was ramped up in 20 s in such a manner that the four quarters correspond to ramps of 0–300 V, 300–600 V, 600–900 V, 900–1500 V, respectively. The image set shown in figure 18(*a*) corresponds to the regime I, which is in response to the application of 0–300 V electric potential. In this regime, upon crossing a threshold voltage, the linear instability is first triggered in the less viscous fluid layer, which grows with the increase in the applied voltage. The characteristics of the instabilities in this regime

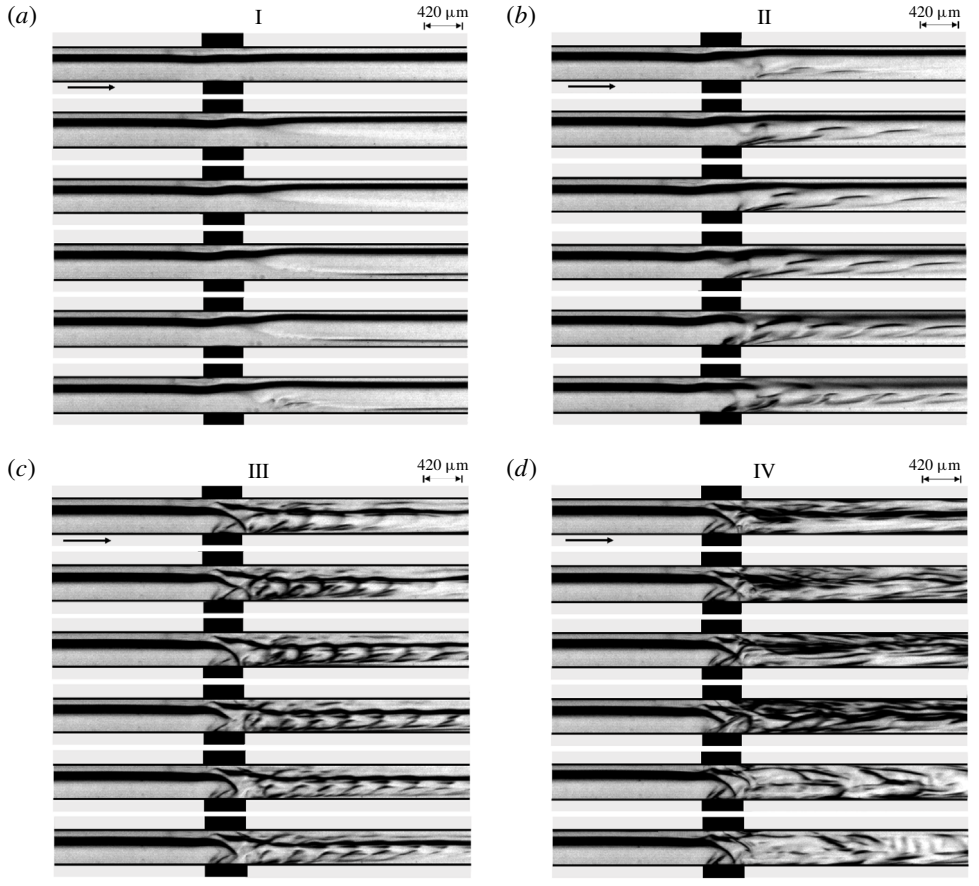

FIGURE 18. Experimental micrographs showing the response of a stratified flow of a benzene–silicone oil system through the channel under application of ramp electric fields of strengths (*a*) 0–300 V, (*b*) 300–600 V, (*c*) 600–900 V and (*d*) 900–1500 V. The first image in the image set (*a*) corresponds to the system under 0 V electric field potential. Four regimes were distinguished, namely I, II, III and IV, as shown on the image sets. The applied voltage was gradually increased from 0 V–1500 V in 20 s, allowing 5 s for stabilization. Experiments were viewed with the help of a microscope under 2.5× magnification under the transmission mode. The videos were recorded at 500 fps. The images correspond to the top view of the flow configuration. The top layer corresponds to benzene and the bottom layer corresponds to silicone oil. The average *Re* maintained during the experiments was 0.5. The arrow indicates the direction of the flow.

have already been discussed in the previous sections. It may be noted here that these instabilities are reversible in nature because turning off the electric field again leads to the formation of the two-layer stratified flow in a short time. The image set in figure 18(*b*) and supporting movie 2 correspond to the regime II, obtained during application of 300–600 V electric potential. This regime is marked by the generation of repeated instability patterns at the downstream of the channel, which qualitatively resemble the time-periodic von Kármán vortex street in appearance. Upon further increase in voltage from 600–900 V, regime III is identified, as shown in the image set in figure 18(*c*) and supporting movie 3. In this situation, the time-periodic flow

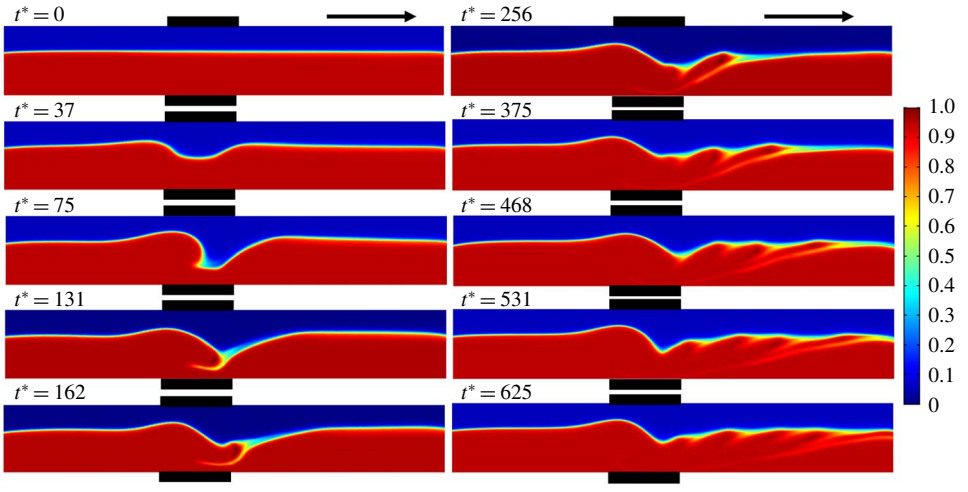

FIGURE 19. (Colour online) Computational snapshots showing the concentration surface plot of a stratified flow of benzene–silicone oil ($V^L = 6$) through the channel at $Ra^\psi = 225$. Here, t^* represents non-dimensional time. The other parameters used for the simulation are $K^L = -4$, $E^L = -0.15$, $Sc = 700$, $I^q = 1$ and $Re = 0.5$. The arrows in the images indicate the direction of the flow. The black rectangles outside the channel represent the electrodes. A positive potential is applied to the top electrode while the bottom electrode is grounded.

patterns start mixing with each other, in addition to having a smaller length scale and higher frequency of ejection of flow structures as compared to regime II. Finally, the voltage increment in the range of 900–1500 V, results in regime IV, depicted in the image set of figure 18(*d*) and supporting movie 4. The images illustrate the onset of a chaotic regime of flow instability where the periodic ejections of flow patterns having higher frequency and smaller length scale intermix to stimulate a ready mixing of the miscible layers.

The CFD simulations also predict qualitatively similar flow structures upon application of an electric field to a stratified flow of two miscible fluids through a channel. Figure 19 and supporting movie 6 depict the concentration surface plot of a stratified flow of benzene–silicone oil ($V^L = 6$) at $Ra^\psi = 225$. The flow is undisturbed at $t^* = 0$ in the absence of an electric field. The EHD instability sets into the system upon application of an electric field, and a vortex street similar to the experimental regimes II and III have been observed in figure 19. The simulations mimic the experimental findings of the reduction of the size and time scale of vortex generation on increasing the electric field, which is depicted in figure 20. The figure shows the concentration surface plots of the benzene–silicone oil system at different values of Ra^ψ. It can be seen from the figure that the sizes of the vortices decrease on increasing Ra^ψ from 225 to 450, accompanied by an increase in the frequency of vortex shedding. This behaviour is qualitatively similar to the experimental observations reported in figure 18. It may be noted here that the simulation results are reproducible with other fluid pairs (different V^L) and also considering liquids with equal ionic mobility ($K^L = 0$), however, the results are not discussed here for the sake of brevity and two such cases are depicted in supporting movies 7 and 8.

In order to characterize regimes II and III shown in figure 18, the frequency of vortex shedding is correlated with the strength of the applied electric field. For this

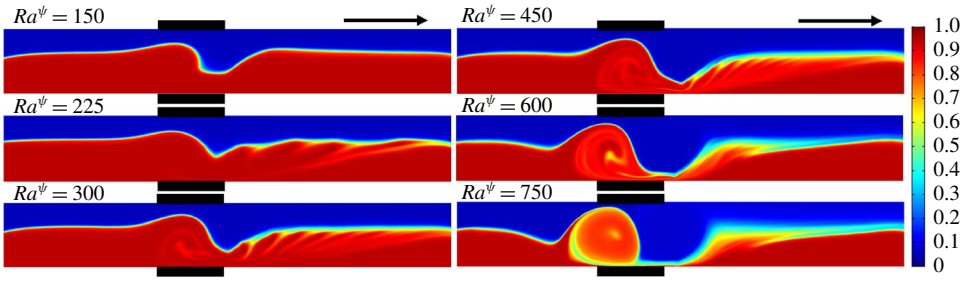

FIGURE 20. (Colour online) Computational snapshots showing the concentration surface plot of a stratified flow of benzene–silicone oil ($V^L = 6$) through the channel at different values of Ra^{ψ} at $t^* = 300$. It may be noted here that t is normalized considering $\Psi_0 =$ 300 V to maintain uniformity in reporting the results. The other parameters used for the simulation are $K^L = -4$, $E^L = -0.15$, $Sc = 700$, $I^q = 1$ and $Re = 0.5$. The arrows in the images indicate the direction of the flow. The black rectangles outside the channel represent the locations of the electrodes. A positive potential is applied to the top electrode while the bottom electrode is grounded.

purpose, we analyse the variation of Strouhal number (St) with electric field Rayleigh number (Ra^{ψ}). The experimental Strouhal number (St) is defined as $St = fR/U$, where f is the frequency of shedding, R is the characteristic length and U is the average flow velocity. In these experiments, the benzene–silicone oil system was subjected to a DC voltage input in the range of 300–850 V at increments of 50 V. The system responded with the generation of vortices, which were recorded and analysed simultaneously. The frequency of the vortex cycles generated per second (f) at each of the applied electric fields was calculated from the frames extracted from the recorded videos. Figure 21 shows the variation of St with Ra^{ψ}, for regimes II and III. The figure suggests that for both regimes II and III, the frequency of vortex generation increases (increasing St) with the strength of the applied field (increasing Ra^{ψ}). The higher values of St in regime III indicate larger frequencies of the vortices as compared to regime II, which can be attributed to a higher electrical force in regime III compared to regime II. Further, regimes II and III can also be differentiated by an abrupt jump observed in the values of St. Interestingly, the experimental time scale of vortex generation, $t_v \sim O(10^{-2}\ \mathrm{s})$, is found to be very close to the theoretical one, $t_v \sim O(10^{-2}\ \mathrm{s}) \sim (RV^L\eta_1)/(K\psi_0 U)$.

We introduce a parameter ξ to quantify the amount of perturbation instilled into the system upon application of electric fields of varying strengths for the regimes I–IV, discussed in figure 18. For this purpose, initially, the benzene–silicone oil system was subjected to DC voltage application in the range of 0–1500 V, at increments of 50 V, and the response was recorded simultaneously. We define, $\xi = 1 - I_e/I_i$, where I_i is the mean grey scale level in absence of an electric field and I_e is the mean grey scale level in the presence of an electric field. The parameter ξ_N represents the normalized values of ξ, obtained by dividing the latter by the maximum value of ξ. The grey scale intensities were measured by image analysis of the extracted frames using the commercial software MATLAB. Figure 22(a) shows the variation of ξ_N with Ra^{ψ}. The ξ_N in this plot were calculated for three distinct regions marked 1, 2 and 3, located upstream, within and downstream of the area of application of the electric field, respectively, as shown in the plot by the rectangular boxes. The intensity values

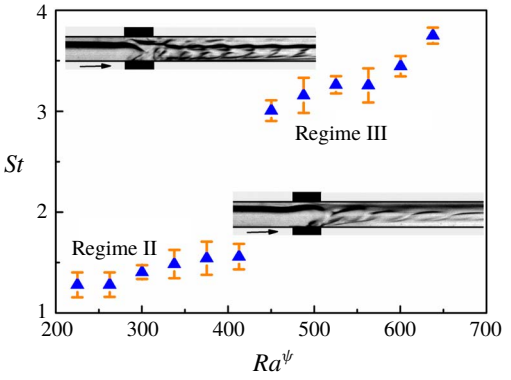

FIGURE 21. (Colour online) Variation of Strouhal number (St) with electric field Rayleigh number (Ra^{ψ}) in regimes II and III, for a benzene–silicone oil system under DC voltage input. The average Re maintained during the experiments was 0.5. The arrow indicates the direction of the flow.

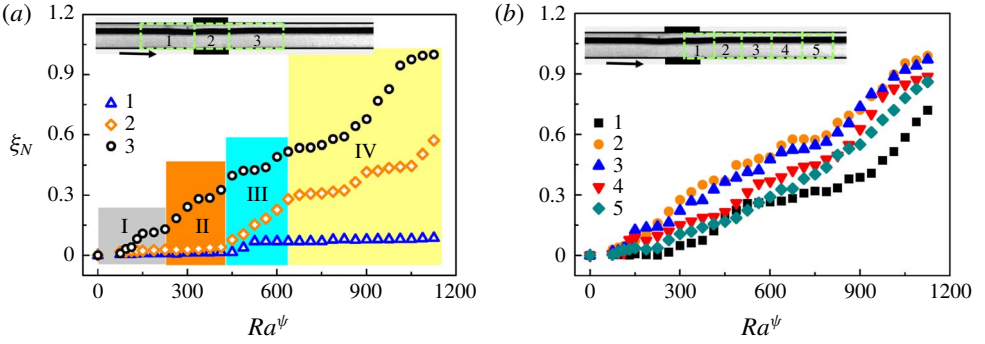

FIGURE 22. (Colour online) (*a*,*b*) Show the variation of perturbation parameter ξ_N with Ra^{ψ}. (*a*) The three regions 1, 2 and 3 in the inset are located at the upstream, within and downstream, of the region where the electric field was applied, respectively. In (*b*), five regions, 1–5, in the inset are identified in the downstream of the region of application of electric field. Regions 1 and 3 in (*a*) are two channels widths in length, and one channel width in breadth. All other regions are squares of one channel width side. The system studied was that of benzene–silicone oil, under application of DC voltages. The average Re maintained during the experiments was 0.5. The arrow indicates the direction of the flow.

represent the mean intensity of all the pixels contained within the regions of interest namely, regions 1, 2 and 3.

The plot suggests that, while ξ_N remains nearly constant at the upstream of the electrodes, the same increases with an increase in Ra^{ψ} within the electrode and downstream regions. Further, at lower values of Ra^{ψ}, when there is little perturbation in the system, the grey scale levels do not change significantly, yielding lower values of ξ_N. With the increase in Ra^{ψ}, the development of the instability modes yield higher values of ξ_N. Region 3 in the downstream, where all the unstable perturbations travel with the fluid, shows a more rapid increase in the values of ξ_N with Ra^{ψ}, as compared to regions 1 and 2. Further, regions 2 and 3 show significantly higher

values of ξ_N in instability regimes III and IV owing to the chaotic nature of the instabilities. Figure 22(*b*) shows the variation of ξ_N with Ra^{ψ} in five different regions immediately downstream to the electrode region, as shown by boxes in the figure. The figure suggests that ξ_N is minimum near region 1, then increases sharply in regions 2 and 3 before again reducing in regions 4 and 5. The plots infer that perturbation strength is maximum in region 2, which is the immediate downstream of the region of application of electric force. The image suggests that the electric field induced perturbations in these systems can only grow up to a certain part of the downstream of the electrodes before they are transported downstream due to pressure-driven flow of the fluid layers. It is important to note here that ξ_N is also a measure of mixing of the fluids in the downstream of the channel. A higher value of ξ_N signifies a larger amount of mixing between the layers. Thus, both the plots in figure 22 suggest that the increase in the electric field intensity can cause a rapid mixing of the fluids at the immediate downstream of the channel. Further, the plots also suggest that the mixing length reduces with the increase in field intensity. The experiments also show that the liquid can immediately be de-mixed when the electric field is turned off, i.e. the perturbations die out immediately upon removal of electric field.

Figures 18–22 show the EHD induced steady, time-periodic and chaotic instabilities in a pressure-driven viscosity stratified flow of a pair of miscible fluids inside a microchannel, which can be employed for rapid mixing of the fluids inside microfluidic devices. The method is found to be reversible in nature because immediate de-mixing of the layers takes place upon the removal of the electric field influence.

Figure 23 and supporting movie 5 show the use of multiple electrodes to cause a rapid mixing of the miscible fluids undergoing a stratified flow inside a microchannel. The optical micrographs (*a–f*) show the response of a benzene–silicone oil stratified flow when a DC voltage of 0–500 V is ramped up through five pairs of electrodes integrated in a staggered manner along the microchannel wall, as shown in the figure. The electrode separation distance in these experiments has been optimized based on the observations made with the single electrode experiments. Again, the top (bottom) layer shown in the image corresponds to benzene (silicone oil). In these experiments, the voltage was ramped up in 5 s to cause the phenomena. All the frames shown in this figure have been extracted from the supporting movie 5. Panel (*a*) corresponds to the pressure-driven situation in absence of the electric field while (*b*) shows the onset of the electric field induced mixing. Panels (*c–f*) show the progressive reduction in the mixing length owing to the generation of time-periodic and unsteady flow patterns with the progressive increase in the field intensity. The multiple electrode arrangement ensure an amplified perturbation in this system induced by the electric field as compared to a single electrode system. Thus, a more efficient mixing of the fluids can be achieved at a much lower voltage in the multi-electrode system. The figure shows the use of the proposed methodology to rapidly mix fluids layers inside the microfluidic devices.

5. Conclusions

A combined theoretical and experimental study uncovers the salient features of electric field induced instabilities associated with the viscosity stratified flow of a pair of miscible fluids inside microchannels. The major conclusions are:

(i) A general linear stability analysis reveals that the EHD instabilities of such systems appear only beyond a critical field intensity. The analysis also uncovers

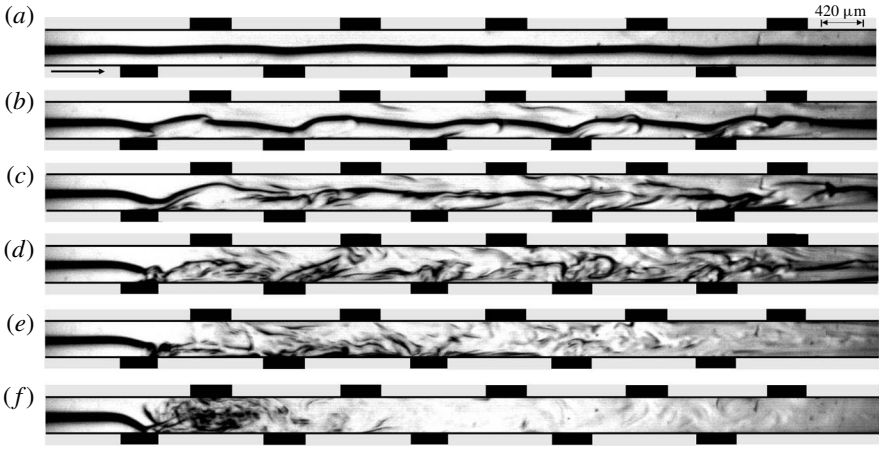

FIGURE 23. Experimental micrographs (*a–f*) show the response of a benzene–silicone oil stratified flow upon application of ramp DC voltage of 0–500 V, through five pairs of electrodes integrated along the channel wall in a staggered fashion. The images correspond to the top view of the flow configuration. The top layer corresponds to benzene and the bottom layer corresponds to silicone oil. (*a*) Corresponds to the system at 0 V. The average *Re* maintained during the experiments was 0.5.

the presence of five distinctive instability modes, which are identified as electric field mode I (E-I), electric field mode II (E-II), viscous mode (V), diffusive mode (D) and the K-mode. Mode E-I appears in the bulk of the lower viscosity fluid at the lower values of Ra^{ψ} while the E-II-mode manifests in the higher viscosity fluid at very high values of Ra^{ψ}. The V-mode appears when the viscosity difference between the fluids is high. Presence of the electric field facilitates the onset of the V-mode when compared with the regular pressure driven flows. The D-mode appears in the mixed interfacial region at higher values of *Sc* due to steep variation of perturbation concentration across the interface. Again, the presence of the electric field facilitates the onset of the D-mode when compared with the regular pressure-driven flows. A contrast of the ionic mobility in the fluids cause the appearance of the much shorter wavelength K-mode.

(ii) The location of the interface (h), thickness of the interface (δ), level of charge injection (I^q), strength of the applied EHD field (Ra^{ψ}), viscosity contrast across the diffused interface (V^L) and diffusivity across the interface (Sc), are found to be some of the very important parameters for these types of instabilities. For relatively small variations in the dielectric constants of the fluids (E^L), the E-I-mode remains nearly unaffected. In particular, the E-I-mode and E-II-mode can be facilitated by increasing the applied field intensity, charge injection levels and reducing the overall viscosity of the fluids. In the linear regime, the experimental and theoretical values obtained for the critical electric field strength, wave speed and wavelength of the E-I-mode of instability are found to be in reasonable qualitative agreement.

(iii) Experiments uncover four distinct regimes of instabilities. The linear regime I corresponds to the onset of instability waves beyond a critical field intensity. With further increase in the applied voltage, the regime II marks the initiation of the nonlinear regime with the appearance of time-periodic vortices in the downstream

of the electrode region. On further increasing the electric field intensity a regime III appears where smaller vortices are generated at higher frequencies leading to intermixing of the flow patterns. The transition of regime II to regime III is marked by an abrupt jump in the Strouhal number. Two-dimensional nonlinear CFD simulations also predict the appearance of vortices which are qualitatively similar to the experimental observations of regime II and III. The simulated results show reduction in size and increment in frequency of shedding with the increase in the electric field intensity. At still higher field intensities, the flow becomes unstructured and chaotic in regime IV leading to total mixing of the two fluids downstream the region of application of electric potential.

(iv) From the perspective of mixing, among all the regimes, the chaotic regime IV with coherent flow patterns is found to be the most suitable one. The mixing is found to happen at the immediate downstream of the electrodes inserted in the channel where electric field can engender a strong intermixing of the layers. The mixing decreases at the far downstream of the channel due to viscous damping of the perturbations induced by the electric field. Interestingly, the mixing and de-mixing processes have been observed to be reversible because the flow immediately restores to its stratified configuration on switching off the electric field. The mixing efficiency is found to increase with the increase in the strength of the applied field and the number of electrodes inserted across the channel.

In summary, the study uncovers a pathway to integrate the influence of an external electrostatic field with a microfluidic device in order to remotely control the mixing of the fluid layers. The phenomenon can be of significance in improving the efficiency of multifarious cutting-edge microfluidic applications which include mixing, pumping, heat exchange, mass transfer and reaction engineering. In depth investigation of the coherent and chaotic regimes, along with a spatial stability analysis of the system has been kept as future scope of research work.

Acknowledgements

We thank DST SERB, grant no. EMR/2016/001824, MeitY-grant no. 5(9)/2012-NANO and the DST-FIST-grant SR/FST/ETII-028/2010, Government of India, for financial aids. We are also grateful for the support from the computer centre for the supercomputing PARAM Ishan facilities at IIT Guwahati. Discussions with Dr S. Timung and Mr J. Chaudhuri are also gratefully acknowledged.

Supplementary movies

Supplementary movies are available at https://doi.org/10.1017/jfm.2018.1023.

Appendix A. Energy analysis

The contributions of the various forces towards production or dissipation of the disturbance kinetic energy are analysed to obtain a more comprehensive understanding of the instability phenomenon. The energy equation is obtained by first multiplying the x and z directional momentum equations (3.3) with the complex conjugate of $\tilde{u}$ ($\tilde{u}^{\dagger}$) and $\tilde{w}$ ($\tilde{w}^{\dagger}$), respectively, then adding the equations, and subsequently, integrating them across the channel length (Selvam *et al.* 2007). The energy equation is given by,

$$E_{KE} = E_{RS} + E_{VD} + E_V + E_E, \tag{A 1}$$

where, E_{KE} represents the rate of change of disturbance kinetic energy, E_{RS} is the energy associated with the Reynolds stress, E_{VD} is the viscous dissipation energy, E_V is the rate of energy change due to viscosity stratification and E_E is the energy associated with the electrical field body force component in the momentum equation. Here,

$$\left.\begin{aligned} E_{KE} &= \omega_r \int_{-1}^{1} (|\tilde{u}|^2 + |\tilde{w}|^2)\,\mathrm{d}z, \\ E_{RS} &= -\int_{-1}^{1} [\mathrm{Re}(\tilde{u}^\dagger \tilde{w}) u_0']\,\mathrm{d}z, \\ E_{VD} &= \frac{1}{Re^\psi} \int_{-1}^{1} \mu_0 [-(|\tilde{u}'|^2 + |\tilde{w}'|^2) - k^2(|\tilde{u}|^2 + |\tilde{w}|^2)]\,\mathrm{d}z, \\ E_{V1} &= \frac{1}{Re^\psi} \int_{-1}^{1} [\mu_0' \{\mathrm{Re}(\tilde{u}^\dagger \tilde{u}' + 2\tilde{w}^\dagger \tilde{w}') + \mathrm{Im}(k\tilde{u}^\dagger \tilde{w})\}]\,\mathrm{d}z, \\ E_{V2} &= \frac{1}{Re^\psi} \int_{-1}^{1} [\tilde{\mu} \{\mathrm{Re}(\tilde{u}^\dagger u_0'') + \mathrm{Im}(k\tilde{w}^\dagger u_0')\}]\,\mathrm{d}z, \\ E_{V3} &= \frac{1}{Re^\psi} \int_{-1}^{1} [\tilde{\mu}' \{\mathrm{Re}(\tilde{u}^\dagger u_0')\}]\,\mathrm{d}z, \\ E_V &= E_{V1} + E_{V2} + E_{V3}, \\ E_E &= \frac{Ra^\psi}{Re^\psi} \int_{-1}^{1} [\mathrm{Im}(k\tilde{u}^\dagger \psi_0'' \tilde{\psi}) + \mathrm{Re}\{\tilde{w}^\dagger (\psi_0'' \tilde{\psi}' + \tilde{\psi}'' \psi_0' - k^2 \psi_0' \tilde{\psi})\}]\,\mathrm{d}z. \end{aligned}\right\} \tag{A 2}$$

Appendix B. Three-dimensional stability analysis

The non-dimensional scheme is given by,

$$\left.\begin{aligned} &(x, y, z, h, \delta) = R(x^*, y^*, z^*, h^*, \delta^*), \quad (u, v, w) = \frac{K\Psi_0}{R}(u^*, v^*, w^*), \\ &\psi = \Psi_0 \psi^*, \quad q = Q_0 q^*, \quad t = \frac{R^2}{K\Psi_0} t^*, \quad p = \frac{\rho K^2 \Psi_0^2}{R^2} p^*, \quad \mu = \mu_1 \mu^*. \end{aligned}\right\} \tag{B 1}$$

Here, u, v and w represent the x, y and z directional velocity components, respectively. The normal linear modes represented by (3.19) are modified as,

$$\begin{aligned} [u, v, w, p, \psi, S, \mu](x, y, z, t) \;=\; & [u_0(z), 0, 0, p_0, \psi_0(z), S_0(z), \mu_0(z)] \\ & + [\tilde{u}, \tilde{v}, \tilde{w}, \tilde{p}, \tilde{\psi}, \tilde{S}, \tilde{\mu}](z) \mathrm{e}^{[\omega t + \mathrm{i}(kx + my)]}. \end{aligned} \tag{B 2}$$

Here, k represents the streamwise and m represents the spanwise wavenumbers, respectively. The non-dimensional linearized momentum equation represented by (3.24) becomes,

$$\begin{aligned} & Re^\psi \mathrm{i}k[(u_0 - c)(\tilde{w}'' - (k^2 + m^2)\tilde{w}) - u_0'' \tilde{w}] \\ & + Ra^\psi (k^2 + m^2)[\psi_0' \tilde{\psi}'' - (\psi_0''' + (k^2 + m^2)\psi_0')\tilde{\psi}] = \mu_0 \tilde{w}'''' + 2\mu_0' \tilde{w}''' \\ & + (\mu_0'' - 2(k^2 + m^2)\mu_0)\tilde{w}'' - 2(k^2 + m^2)\mu_0' \tilde{w}' + ((k^2 + m^2)\mu_0'' + (k^2 + m^2)^2 \mu_0)\tilde{w} \\ & - \mathrm{i}ku_0' \tilde{\mu}'' - 2\mathrm{i}ku_0'' \tilde{\mu}' - (\mathrm{i}ku_0''' + \mathrm{i}k(k^2 + m^2)u_0')\tilde{\mu}. \end{aligned} \tag{B 3}$$

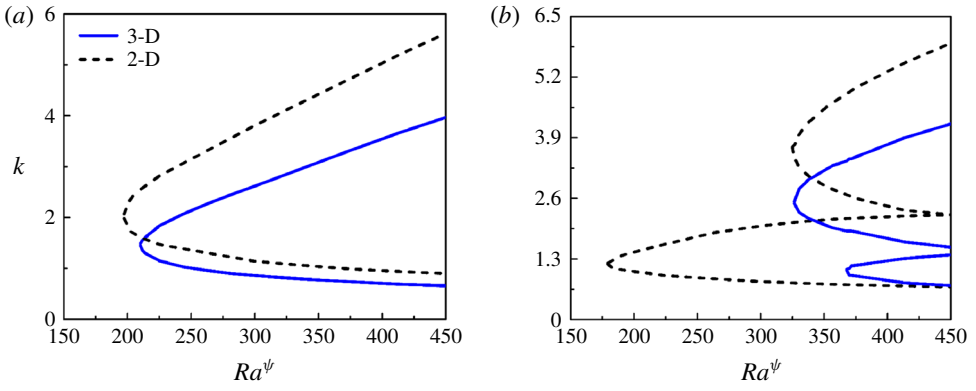

FIGURE 24. (Colour online) Neutral stability curves (*a*,*b*) show the variation of streamwise wavenumber (k) with electric Rayleigh number (Ra^{ψ}) for two-dimensional (evenly broken line) and three-dimensional (solid line) perturbations. The other parameters for (*a*) are $V^L = 1$, $h = 0$, $\delta = 0.02$, $Sc = 10$ and $Re = 0.5$. The other parameters for (*b*) are $V^L = 3$, $h = -0.3$, $\delta = 0.02$, $Sc = 10$ and $Re = 0.5$. The value of the spanwise wavenumber m is set equal to k for the three-dimensional cases.

The charge conservation equation (3.25) is modified as,

$$\mathrm{i}k\left[(u_0 - c)(\tilde{\psi}'' - (k^2 + m^2)\tilde{\psi}) - \frac{\mathrm{i}}{k}\psi_0'''\tilde{w}\right] = \psi_0'\tilde{\psi}''' + 2\psi_0''\tilde{\psi}'' + (\psi_0''' - (k^2 + m^2)\psi_0')\tilde{\psi}' - 2(k^2 + m^2)\psi_0''\tilde{\psi}. \tag{B 4}$$

The advection–diffusion equation of the concentration scalar becomes,

$$\mathrm{i}kRe^{\psi}Sc\left[(u_0 - c)\tilde{S} - \frac{\mathrm{i}}{k}S_0'\tilde{w}\right] = \tilde{S}'' - (k^2 + m^2)\tilde{S}. \tag{B 5}$$

Equations (B 3)–(B 5) are solved using the boundary conditions mentioned in (3.27)–(3.29) and applying the numerical methodology mentioned in § 3.4.3 of the main text. Figure 24 shows the comparison between neutral stability plots of the two-dimensional and three-dimensional perturbations. It may be noted that for the three-dimensional cases, $m = k$ is considered. Figure 24(*a*) shows that the two dimensional perturbations are unstable at a lower value of critical Ra^{ψ} compared to the three-dimensional perturbations. Figure 24(*b*) also depicts a similar trend with the two-dimensional perturbations being more unstable than the three-dimensional ones. Thus, in the light of the above observation, it is evident that two-dimensional perturbations become unstable at lower values of Ra^{ψ}, compared to the three-dimensional ones. Hence, only two-dimensional transversal modes are considered in the analysis.

Appendix C. Estimation of thickness of mixed layer δ

For the diffusion process, the length scale can be approximated as, $\delta \sim \sqrt{\kappa t}$. The diffusion coefficient $\kappa \sim O(10^{-9} - 10^{-11})$ m^2 s^{-1} (Petitjeans & Maxworthy 1996; Lajeunesse *et al.* 1999), the time scale t can be approximated as, $t \sim O(10^{-1} - 10^{-2})$ s.

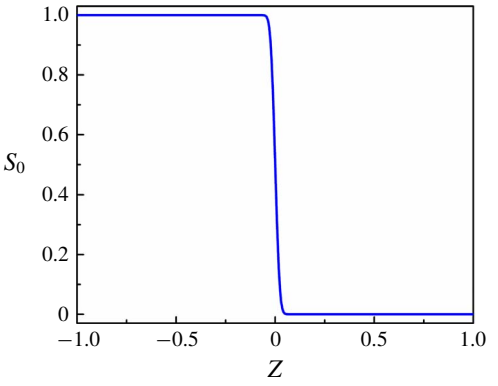

FIGURE 25. (Colour online) The variation of concentration scalar (S_0) across the channel at the base state. The parameters considered for the simulation are $h = 0$, $Sc = 700$ and $V^L = 6$.

Thus, δ is obtained as $\delta \sim O(10^{-5} - 10^{-6})$ m. This gives the dimensionless value of $\delta \sim O(10^{-1} - 10^{-2})$ considering the characteristic length to be $\sim 10^{-4}$ m. It was further confirmed through the nonlinear CFD simulations, the details of which are mentioned in § 3.5. Figure 25 shows the base-state scalar (S_0) profile, for $V^L = 6$. It can be seen from the figure that the thickness of the mixed interface at the base state is ~ 0.05.

REFERENCES

ALJ, A., DENAT, A., GOSSE, J. P., GOSSE, B. & NAKAMURA, I. 1985 Creation of charge carriers in nonpolar liquids. *IEEE Trans. Electr. Insul.* **EI-20** (2), 221–231.

ALLEN, P. H. G. & KARAYIANNIS, T. G. 1995 Electrohydrodynamic enhancement of heat transfer and fluid flow. *Heat Recov. Syst. CHP* **15** (5), 389–423.

ATTEN, P. 1974 Electrohydrodynamic stability of dielectric liquids during transient regime of space-charge-limited injection. *Phys. Fluids* **17** (10), 1822–1827.

ATTEN, P. & GOSSE, J. P. 1969 Transient of one-carrier injections in polar liquids. *J. Chem. Phys.* **51** (7), 2804–2811.

ATTEN, P. & HAIDARA, M. 1985 Electrical conduction and EHD motion of dielectric liquids in a knife-plane electrode assembly. *IEEE Trans. Electr. Insul.* **E1-20** (2), 187–198.

ATTEN, P. & LACROIX, J. C. 1979 Non-linear hydrodynamic stability of liquids subjected to unipolar injection. *J. Méc.* **18**, 469–510.

ATTEN, P. & MOREAU, R. 1972 Stabilité électrohydrodynamique des liquides isolants soumis à une injection unipolaire. *J. Méc.* **11** (3), 471–521.

BART, S. F., TAVROW, L. S., MEHREGANY, M. & LANG, J. H. 1990 Microfabricated electrohydrodynamic pumps. *Sensor Actuators* A **21** (1), 193–197.

BERTSCH, A., HEIMGARTNER, S., COUSSEAU, P. & RENAUD, P. 2001 Static micromixers based on large-scale industrial mixer geometry. *Lab on a Chip* **1** (1), 56–60.

BOBYL, V. G., ROMANETS, R. G. & ALYAB'EV, V. A. 1965 The electrical conductivity of benzene and its monohalide derivatives in an ultrasonic field. *Sov. Phys. J.* **8**, 30–34.

BROMBERG, A. & MATHIES, R. A. 2003 Homogeneous immunoassay for detection of TNT and its analogues on a microfabricated capillary electrophoresis chip. *Anal. Chem.* **75** (5), 1188–1195.

CASTELLANOS, A 1991 Coulomb-driven convection in electrohydrodynamics. *IEEE Trans. Electr. Insul.* **26** (6), 1201–1215.

CASTELLANOS, A. & AGRAIT, N. 1992 Unipolar injection induced instabilities in plane parallel flows. *IEEE Trans Ind. Applics.* **28** (3), 513–519.

CHAKRABORTY, S., LIAO, I.-C., ADLER, A. & LEONG, K. W. 2009 Electrohydrodynamics: a facile technique to fabricate drug delivery systems. *Adv. Drug Deliv. Rev.* **61** (12), 1043–1054.

CHEN, C.-H., LIN, H., LELE, S. K. & SANTIAGO, J. G. 2005 Convective and absolute electrokinetic instability with conductivity gradients. *J. Fluid Mech.* **524**, 263–303.

CHEN, C.-Y. & MEIBURG, E. 1996 Miscible displacements in capillary tubes. Part 2. Numerical simulations. *J. Fluid Mech.* **326**, 57–90.

CHRISTODOULIDES, N., TRAN, M., FLORIANO, P. N., RODRIGUEZ, M., GOODEY, A., ALI, M., NEIKIRK, D. & MCDEVITT, J. T. 2002 A microchip-based multianalyte assay system for the assessment of cardiac risk. *Anal. Chem.* **74** (13), 3030–3036.

CRAIK, A. D. D. 1969 The stability of plane Couette flow with viscosity stratification. *J. Fluid Mech.* **36** (4), 685–693.

DENAT, A., GOSSE, B. & GOSSE, J. P. 1979 Ion injections in hydrocarbons. *J. Electrostat.* **7**, 205–225.

DING, Z. & WONG, T. N. 2015 Electrohydrodynamic instability of miscible coreannular flows with electrical conductivity stratification. *J. Fluid Mech.* **764**, 488–512.

DOYLE, P. S., BIBETTE, J., BANCAUD, A. & VIOVY, J.-L. 2002 Self-assembled magnetic matrices for dna separation chips. *Science* **295** (5563), 2237.

EL MOCTAR, A. O., AUBRY, N. & BATTON, J. 2003 Electro-hydrodynamic micro-fluidic mixer. *Lab on a Chip* **3** (4), 273–280.

ERN, P., CHARRU, F. & LUCHINI, P. 2003 Stability analysis of a shear flow with strongly stratified viscosity. *J. Fluid Mech.* **496**, 295–312.

GHOSH, S. & USHA, R. 2016 Stability of viscosity stratified flows down an incline: role of miscibility and wall slip. *Phys. Fluids* **28**, 104101.

GOVINDARAJAN, R. 2004 Effect of miscibility on the linear instability of two-fluid channel flow. *Intl J. Multiphase Flow* **30** (10), 1177–1192.

HAEBERLE, S. & ZENGERLE, R. 2007 Microfluidic platforms for lab-on-a-chip applications. *Lab on a Chip* **7**, 1094–1110.

HARNETT, C. K, TEMPLETON, J., DUNPHY-GUZMAN, K. A., SENOUSY, Y. M. & KANOUFF, M. P. 2008 Model based design of a microfluidic mixer driven by induced charge electroosmosis. *Lab on a Chip* **8** (4), 565–572.

HERTZOG, D. E., IVORRA, B., MOHAMMADI, B., BAKAJIN, O. & SANTIAGO, J. G. 2006 Optimization of a microfluidic mixer for studying protein folding kinetics. *Anal. Chem.* **78** (13), 4299–4306.

HIGUERA, F. J. 2002 Electrohydrodynamic flow of a dielectric liquid due to autonomous injection of charge by a needle electrode. *Phys. Fluids* **14** (1), 423–426.

HINSMANN, P., FRANK, J., SVASEK, P., HARASEK, M. & LENDL, B. 2001 Design, simulation and application of a new micromixing device for time resolved infrared spectroscopy of chemical reactions in solution. *Lab on a Chip* **1** (1), 16–21.

HOPFINGER, E. J. & GOSSE, J. P. 1971 Charge transport by selfgenerated turbulence in insulating liquids submitted to unipolar injection. *Phys. Fluids* **14** (8), 1671–1682.

JANASEK, D., FRANZKE, J. & MANZ, A. 2006 Scaling and the design of miniaturized chemical-analysis systems. *Nature* **442** (7101), 374.

JHA, B., CUETO-FELGUEROSO, L. & JUANES, R. 2011 Fluid mixing from viscous fingering. *Phys. Rev. Lett.* **106** (19), 194502.

KO, S. H., LEE, H. & KANG, K. H. 2008 Hydrodynamic flows in electrowetting. *Langmuir* **24** (3), 1094–1101.

LACROIX, J. C., ATTEN, P. & HOPFINGER, E. J. 1975 Electro-convection in a dielectric liquid layer subjected to unipolar injection. *J. Fluid Mech.* **69** (3), 539–563.

LAJEUNESSE, E., MARTIN, J., RAKOTOMALALA, N., SALIN, D. & YORTSOS, Y. C. 1999 Miscible displacement in a Hele-Shaw cell at high rates. *J. Fluid Mech.* **398**, 299–319.

LARA, J. L., CASTELLANOS, A. & PONTIGA, F. 1997 Destabilization of plane Poiseuille flow of insulating liquids by unipolar charge injection. *Phys. Fluids* **9** (2), 399–406.

VAN DER MAESEN, F. 1949 The absolute dielectric constant of benzene. *Physica* **15** (5–6), 481–483.

MALRAISON, B. & ATTEN, P. 1982 Chaotic behavior of instability due to unipolar ion injection in a dielectric liquid. *Phys. Rev. Lett.* **49** (10), 723–726.

MARK, D., HAEBERLE, S., ROTH, G., VON STETTEN, F. & ZENGERLE, R. 2010 Microfluidic lab-on-a-chip platforms: requirements, characteristics and applications. *Chem. Soc. Rev.* **39**, 1153–1182.

MCCLUSKEY, F. M. J., ATTEN, P. & PEREZ, A. T. 1991 Heat transfer enhancement by electroconvection resulting from an injected space charge between parallel plates. *Intl J. Heat Mass Transfer* **34** (9), 2237–2250.

MCCLUSKEY, F. M. J. & ATTEN, P. 1988 Modifications to the wake of a wire across Poiseuille flow due to a unipolar space charge. *J. Fluid Mech.* **197**, 81–104.

ODDY, M. H., SANTIAGO, J. G. & MIKKELSEN, J. C. 2001 Electrokinetic instability micromixing. *Anal. Chem.* **73** (24), 5822–5832.

D'OLCE, M., MARTIN, J., RAKOTOMALALA, N., SALIN, D. & TALON, L. 2009 Convective/absolute instability in miscible core-annular flow. Part 1. Experiments. *J. Fluid Mech.* **618**, 305–322.

OLIVERI, S., ATTEN, P. & CASTELLANOS, A. 1987 The stability of a planar layer of insulating liquid subjected to charge injection and rotation. *Phys. Fluids* **30** (7), 1948–1955.

ORSZAG, S. A. 1971 Accurate solution of the Orr-Sommerfeld stability equation. *J. Fluid Mech.* **50** (4), 689–703.

OTSUBO, Y. & EDAMURA, K. 1998 Viscoelasticity of a dielectric fluid in nonuniform electric fields generated by electrodes with flocked fabrics. *Rheol. Acta* **37** (5), 500–507.

PETITJEANS, P. & MAXWORTHY, T. 1996 Miscible displacements in capillary tubes. Part 1. Experiments. *J. Fluid Mech.* **326**, 37–56.

PONTIGA, F., CASTELLANOS, A. & MALRAISON, B. 1995 Some considerations on the instabilities of nonpolar liquids subjected to charge injection. *Phys. Fluids* **7** (6), 1348–1356.

POSNER, J. D., PÉREZ, C. L. & SANTIAGO, J. G. 2012 Electric fields yield chaos in microflows. *Proc. Natl Acad. Sci. USA* **109** (36), 14353–14356.

POSNER, J. D. & SANTIAGO, J. G. 2006 Convective instability of electrokinetic flows in a cross-shaped microchannel. *J. Fluid Mech.* **555**, 1–42.

PREZIOSI, L., CHEN, K. & JOSEPH, D. D. 1989 Lubricated pipelining: stability of core-annular flow. *J. Fluid Mech.* **201**, 323–356.

RANGANATHAN, B. T. & GOVINDARAJAN, R. 2001 Stabilization and destabilization of channel flow by location of viscosity-stratified fluid layer. *Phys. Fluids* **13** (1), 1–3.

REN, Q. Y., WANG, L. F. & HUANG, Q. A. 2016 A new method for real-time measuring the temperature-dependent dielectric constant of the silicone oil. *IEEE Sens. J.* **16** (24), 8792–8797.

RHEE, S. W., TAYLOR, A. M., TU, C. H., CRIBBS, D. H., COTMAN, C. W. & JEON, N. L. 2005 Patterned cell culture inside microfluidic devices. *Lab on a Chip* **5**, 102–107.

RIFE, J. C., BELL, M. I., HORWITZ, J. S., KABLER, M. N., AUYEUNG, R. C. Y. & KIM, W. J. 2000 Miniature valveless ultrasonic pumps and mixers. *Sens. Actuat. A: Phys.* **86** (1), 135–140.

SAHU, K. C. & GOVINDARAJAN, R. 2016 Linear stability analysis and direct numerical simulation of two-layer channel flow. *J. Fluid Mech.* **798**, 889–909.

SAMIEI, E., TABRIZIAN, M. & HOORFAR, M. 2016 A review of digital microfluidics as portable platforms for lab-on a-chip applications. *Lab on a Chip* **16**, 2376–2396.

SCHMID, P. J. & HENNINGSON, D. S. 2001 *Stability and Transition in Shear Flows*. Springer.

SCHMIDT, W. F. & YOSHINO, K. 2015 Ion mobilities in non-polar dielectric liquids: silicone oils. *IEEE Trans. Dielec. Elec. Insul.* **22** (5), 2424–2427.

SCHNEIDER, J. M. & WATSON, P. K. 1970 Electrohydrodynamic stability of space-charge-limited currents in dielectric liquids. I. Theoretical study. *Phys. Fluids* **13** (8), 1948–1954.

SCOFFONI, J., LAJEUNESSE, E. & HOMSY, G. M. 2001 Interface instabilities during displacements of two miscible fluids in a vertical pipe. *Phys. Fluids* **13** (3), 553–556.

SELVAM, B., MERK, S., GOVINDARAJAN, R. & MEIBURG, E. 2007 Stability of miscible core–annular flows with viscosity stratification. *J. Fluid Mech.* **592**, 23–49.

SELVAM, B., TALON, L., LESSHAFFT, L. & MEIBURG, E. 2009 Convective/absolute instability in miscible core-annular flow. Part 2. Numerical simulations and nonlinear global modes. *J. Fluid Mech.* **618**, 323–348.

SIMONNET, C. & GROISMAN, A. 2005 Chaotic mixing in a steady flow in a microchannel. *Phys. Rev. Lett.* **94** (13), 134501.

SKOTAK, M. & LARSEN, G. 2006 Solution chemistry control to make well defined submicron continuous fibres by electrospinning: the $(CH_3CH_2CH_2O)_4Ti$/AcOH/poly(*N*-vinylpyrrolidone) system. *J. Mater. Chem.* **16**, 3031–3039.

DE SOUSA, F. F., MOREIRA, S. G. C., SHIRSLEY, J., NERO, J. D. & ALCANTARA, P. JR. 2009 Dielectric properties of oleic acid in liquid phase. *J. Bionanoscience* **3** (2), 139–142.

SPOHNER, M. 2016 Study of the dielectric properties of vegetable oils and their constituents. In *Diagnostic of Electrical Machines and Insulating Systems in Electrical Engineering (DEMISEE)*, pp. 16–19. IEEE.

STONE, H. A., STROOCK, A. D. & AJDARI, A. 2004 Engineering flows in small devices: microfluidics toward a lab-on-a-chip. *Annu. Rev. Fluid Mech.* **36**, 381–411.

STROOCK, A. D., DERTINGER, S. K. W., AJDARI, A., MEZIĆ, I., STONE, H. A. & WHITESIDES, G. M. 2002 Chaotic mixer for microchannels. *Science* **295** (5555), 647–651.

SUH, Y. K. 2012 Modeling and simulation of ion transport in dielectric liquids – fundamentals and review. *IEEE Trans. Dielec. Elec. Insul.* **19** (3), 831–848.

TALON, L., GOYAL, N. & MEIBURG, E. 2013 Variable density and viscosity, miscible displacements in horizontal Hele-Shaw cells. Part 1. Linear stability analysis. *J. Fluid Mech.* **721**, 268–294.

TALON, L. & MEIBURG, E. 2011 Plane poiseuille flow of miscible layers with different viscosities: instabilities in the Stokes flow regime. *J. Fluid Mech.* **686**, 484–506.

TAN, C. T. & HOMSY, G. M. 1986 Stability of miscible displacements in porous media: rectilinear flow. *Phys. Fluids* **29** (11), 3549–3556.

TIMUNG, S., CHAUDHURI, J., BORTHAKUR, M. P., MANDAL, T. K., BISWAS, G. & BANDYOPADHYAY, D. 2017 Electric field mediated spraying of miniaturized droplets inside microchannel. *Electrophoresis* **38** (11), 1450–1457.

TOBAZEON, R., HAIDARA, M. & ATTEN, P. 1984 Ion injection and kerr plots in liquids with blade-plane electrodes. *J. Phys.* D*: Appl. Phys.* **17** (6), 1293–1301.

TRAORÉ, P. & PÉREZ, A. T. 2012 Two-dimensional numerical analysis of electroconvection in a dielectric liquid subjected to strong unipolar injection. *Phys. Fluids* **24** (3), 037102.

TSUKAHARA, Y., HIROSE, Y. & OTSUBO, Y. 2013 Effect of electrode materials on electrohydrodynamic flows of ethanol. *Colloids Surf.* A **425**, 76–82.

VASILKOV, S. A., CHIRKOV, V. A. & STISHKOV, Y. K. 2017 Study on high-voltage conductivity provided solely by field-enhanced dissociation in liquid dielectrics. *J. Electrostat.* **88**, 81–87.

VÁZQUEZ, P. A., GEORGHIOU, G. E. & CASTELLANOS, A. 2006 Characterization of injection instabilities in electrohydrodynamics by numerical modelling: comparison of particle in cell and flux corrected transport methods for electroconvection between two plates. *J. Phys.* D*: Appl. Phys.* **39** (13), 2754–2763.

VERMA, M. K. S., GANNEBOYINA, S. R., VINAYAK, R. R. & GHATAK, A. 2008 Three-dimensional multihelical microfluidic mixers for rapid mixing of liquids. *Langmuir* **24** (5), 2248–2251.

VILKNER, T., JANASEK, D. & MANZ, A. 2004 Micro total analysis systems. Recent developments. *Anal. Chem.* **76** (12), 3373–3386.

WALL, D. P. & WILSON, S. K. 1996 The linear stability of channel flow of fluid with temperature-dependent viscosity. *J. Fluid Mech.* **323**, 107–132.

WANG, B. F. & SHEU, T. W. H. 2016 Numerical investigation of electrohydrodynamic instability and bifurcation in a dielectric liquid subjected to unipolar injection. *Comput. Fluids* **136**, 1–10.

WANG, G., YANG, F., ZHAO, W. & CHEN, C.-P. 2016 On micro-electrokinetic scalar turbulence in microfluidics at a low Reynolds number. *Lab on a Chip* **16** (6), 1030–1038.

WANG, G. R., YANG, F. & ZHAO, W. 2014 There can be turbulence in microfluidics at low Reynolds number. *Lab on a Chip* **14** (8), 1452–1458.

WANG, J., IBÁÑEZ, A., CHATRATHI, M. P. & ESCARPA, A. 2001 Electrochemical enzyme immunoassays on microchip platforms. *Anal. Chem.* **73** (21), 5323–5327.

WATSON, P. K., SCHNEIDER, J. M. & TILL, H. R. 1970 Electrohydrodynamic stability of space-charge-limited currents in dielectric liquids. II. Experimental study. *Phys. Fluids* **13** (8), 1955–1961.

WEIDEMAN, J. A. & REDDY, S. C. 2000 A matlab differentiation matrix suite. *ACM Trans. Math. Softw.* **26** (4), 465–519.

WU, J., PÉREZ, A. T., TRAORÉ, P. & VÁZQUEZ, P. A. 2015 Complex flow patterns at the onset of annular electroconvection in a dielectric liquid subjected to an arbitrary unipolar injection. *IEEE Trans. Dielec. Elec. Insul.* **22** (5), 2637–2645.

WU, J., TRAORÉ, P., VÁZQUEZ, P. A. & PÉREZ, A. T. 2013 Onset of convection in a finite two-dimensional container due to unipolar injection of ions. *Phys. Rev.* E **88**, 053018.

YI, M., QIAN, S. & BAU, H. H. 2002 A magnetohydrodynamic chaotic stirrer. *J. Fluid Mech.* **468**, 153–177.

ZHANG, H. B., EDIRISINGHE, M. J. & JAYASINGHE, S. N. 2006 Flow behaviour of dielectric liquids in an electric field. *J. Fluid Mech.* **558**, 103–111.

ZHANG, M. 2016 Weakly nonlinear stability analysis of subcritical electrohydrodynamic flow subject to strong unipolar injection. *J. Fluid Mech.* **792**, 328–363.

ZHANG, M., MARTINELLI, F., WU, J., SCHMID, P. J. & QUADRIO, M. 2015 Modal and non-modal stability analysis of electrohydrodynamic flow with and without cross-flow. *J. Fluid Mech.* **770**, 319–349.

ZHAO, H. & BAU, H. H. 2007 Microfluidic chaotic stirrer utilizing induced-charge electro-osmosis. *Phys. Rev.* E **75** (6), 066217.